

Sol-Gel Derived Nanocrystalline Fluoridated Hydroxyapatite Powders and Nanostructured Coatings for Tissue Engineering Applications

E. MOHAMMADI ZAHRANI, M.H. FATHI, and A.M. ALFANTAZI

Nanocrystalline fluoridated hydroxyapatite (FHA) powders and coatings with a chemical composition of $\text{Ca}_{10}(\text{PO}_4)_6\text{OH}_{2-x}\text{F}_x$ (where x values were selected equal to 0.0, 0.5, 1.0, 1.5, and 2.0) were prepared through a modified simple sol-gel technique in comparison with conventional alkoxide-based sol-gel route. X-ray diffraction (XRD), transmission electron microscopy (TEM), scanning electron microscopy (SEM), fourier transform infrared (FTIR) spectroscopy, pF-meter with a fluorine-sensitive electrode, and inductively coupled plasma-optical emission spectroscopy (ICP-OES) analysis techniques were employed in order to evaluate phase composition, particle size distribution, morphology, functional groups, fluorine content, and purity of prepared FHA nanopowders, respectively. SEM analysis was used to study the surface morphology and cross section of the FHA coatings, deposited on 316L stainless steel substrate. Results indicated that single-phase and homogeneous FHA nanopowders with carbonate peaks in the FTIR spectrum were synthesized through the modified sol-gel technique. TEM analysis revealed that fluorapatite (FA) powder was composed of nanosized particles, ~25 nm in size, with polyhedron shape and straight corners. In the modified sol-gel technique, polymerization and gelation kinetic of the sol were significantly improved without any need to use additives or pH control. Uniform, dense, well-adhered, and compacted FHA coatings were formed on the 316L stainless steel substrate after 24 hours of aging.

DOI: 10.1007/s11661-010-0465-2

© The Minerals, Metals & Materials Society and ASM International 2010

I. INTRODUCTION

HUMAN body hard tissue is a nanocomposite consisting of mineral phases, collagen fibers, and proteins. Naturally derived nanocrystalline apatite is the main mineral phase of hard tissue embedded in biologically produced organic matrix.^[1] Biological apatite has attracted a great deal of attention because of the presence of trace elements, which do not change the basic crystallographic characteristics of apatite^[2,3] but can improve the overall biological performance of implant material. Bone minerals contain considerable amounts of fluoride ions (ca. 0.04 to 0.07 wt pct), carbonate (ca. 4 to 8 wt pct), sodium (ca. 0.7 wt pct), magnesium (ca. 0.55 wt pct), and potassium (ca. 0.03 wt pct).^[2,4] In comparison, carbonate and fluoride play the most leading role because of their influence on the physical and biological properties of the mineral phase of bone and teeth. In particular, the presence of fluorine in saliva and blood plasma is important for normal skeletal and dental development.^[5]

It was found that fluoride is uniformly distributed within bone tissue or within the thin tooth enamel outer layer, where the degree of fluoridation may be as high as $x = 1$ (fluoridated hydroxyapatite (FHA): $\text{Ca}_{10}(\text{PO}_4)_6\text{OH}_{2-x}\text{F}_x$, where x stands for the degree of fluoridation). Fluorine ion itself has a crucial effect in promoting the rate of biological crystal growth, facilitating biological minerals crystallization, and transformation and enhances remineralization, by adsorbing to the enamel surface and attracting calcium ions, and retards demineralization of teeth.^[6,7] Partially FHA could be used to increase the bone mass in a regular fashion without any formation of mineralization defects.^[5]

FHA has attracted much attention as a promising material to replace hydroxyapatite (HA) in biomedical bone scaffolding applications, especially when excellent integration in bone/tissue interface and long-term performance of the implant are needed.^[8] In the last decade, some studies were extended to the synthesis of solid solution FHA to be used in the form of powder,^[9] composite,^[10,13] tissue engineering scaffold,^[11] or surface coating^[12] on various orthopaedic prostheses and dental implants. Fluorine plays a significant role in stimulating bone-derived cellular activity^[13] and enhancing bone union *in vivo*. Biodegradation of HA coating under physiological conditions is the most important restricting factor in biomedical application, since it makes the interface between coated implant and hard tissue unstable. Incorporation of fluorine ions into the HA structure

E. MOHAMMADI ZAHRANI, PhD Student, and A.M. ALFANTAZI, Associate Professor, are with the Department of Materials Engineering, The University of British Columbia, Vancouver, BC V6T 1Z4, Canada. Contact e-mail: ehsanmoh@interchange.ubc.ca M.H. FATHI, Professor, is with the Biomaterials Group, Department of Materials Engineering, Isfahan University of Technology, Isfahan 84156-83111, Iran.

Manuscript submitted March 11, 2010.

Article published online December 3, 2010

significantly enhances the resistance of HA to biodegradation, as a positive factor for a prospective application, e.g., in bone drug delivery systems.^[8] Moreover, FHA could provide better protein adsorption and comparable or better cell attachment than HA,^[14] and it showed notable resistance to corrosion and thermal decomposition.^[8] Replacement of OH⁻¹ groups in the apatite structure with F⁻¹ ions also has positive effects on proliferation, alkaline phosphate activity (ALP), morphology, differentiation, and density of osteoblastic-like cells and promotes bioactivity.^[15] Fairly *et al.* showed that fluoride could increase osteoblast formation in embryonic calvaria at concentrations that stimulated bone formation *in vivo*.^[16] Micromolar level of fluoride ion could increase the activity of mature osteoblasts, synthesis of collagen, and osteocalcin (OC).^[13,17] The relative mechanism has not been well understood, but based on the report of Yan *et al.*,^[18] fluoride effects on osteoclastogenesis have been demonstrated to be influenced by the genetic background, and the cumulative result of these effects is a net increase in bone formation. It was confirmed that the bone-associated gene expression level of ALP and OC in the osteoblast cells was up-regulated when F⁻¹ ions were incorporated into the apatite structure.^[13] Moreover, FHA promotes new mineralization of incipient lesions and also it could prevent, reduce, and control dental caries.^[19]

Various techniques have been developed for the synthesis of FHA nanopowders. The main techniques being used include precipitation,^[8] hydrolysis,^[20] hydrothermal,^[21,22] pH cycling,^[23] sol-gel,^[14,15,24-27] electrochemical deposition,^[28] and mechanical alloying^[29] processing routes. In comparison, sol-gel is the most promising technique for preparation of highly pure FHA nanopowders and nanostructured coatings due to the possibility of precise control of process parameters.^[15] Sol-gel techniques have many merits such as molecular mixing of the initial materials, which improves chemical homogeneity, low cost, the ability to generate nanosized particles, and nanostructured coatings on various metallic and ceramic substrates as well as the possibility of ion incorporation into the structure. The sol-gel derived bioceramics such as HA or FA are characterized by low crystallization temperature, because of the high reactivity of sol-gel derived powders, and nanosize dimension of primary particles, an important parameter to improving the contact reaction and stability in the implant/natural bone interface.^[30] However, different sol-gel approaches studied so far for FHA preparation^[14,15,24-27] still have some shortcomings, most significantly, the need for several complicated steps to ensure complete dissolution and hydrolysis of precursors to generate pure FHA phase after post heat treatment, strict pH control to avoid precipitation in initial sol, and extended vigorous agitation. Moreover, it seems that in all sol-gel methods, chemical hydrolysis reactions and polymerization in the sol, required for gelation and final product formation, could not be completely done in a reasonable time without addition of an acidic catalyst. Therefore, there is still an important need to identify a modified sol-gel approach, which is simple and comprises steps that could be easily

employed without any need for following stringent procedures, careful manipulations, or catalyst addition.

Therefore, in this work, a modified simple sol-gel approach was employed using usually available and inexpensive precursors to generate FHA nanopowders and perform nanostructured FHA coatings on 316L stainless steel substrate. By employing this technique, FHA gel formation took place faster, aging time was reduced, and gel was simply achieved without prolonged refluxing steps of precursor's alcoholic solution, pH control during sol titration, or addition of catalyst. In this modified approach, designed amounts of fluorine were completely incorporated into the apatite structure and gelation and polymerization behavior and kinetic were significantly improved, compared to the conventional alkoxide-based sol-gel technique.

II. EXPERIMENTAL PROCEDURE

A. Modified Sol-Gel Approach ("Method A")

The flowchart of modified approach can be seen in Figure 1(a). Also, predetermined amounts of calcium, phosphorous, and flour precursors used for preparation of initial FHA sols are presented in Table I. In summary, for each FHA sample, first, a predetermined amount of phosphorous pentoxide (P₂O₅, Merck, Germany) was added into a beaker and 20 mL of absolute ethanol (Merck) was immediately added. After that, calcium nitrate tetrahydrate (Ca(NO₃)₂·4H₂O, Merck) and 20 mL of absolute ethanol were added to the solution. Then, hexafluorophosphoric acid (HPF₆, Sigma-Aldrich, St-Louis, MO) as a fluorine-containing reagent was added into the mixture. Finally, the mixture with a Ca/P molar ratio equal to 1.67 was continuously stirred at room temperature until a highly viscous gel formed. The addition sequence of the precursors is important and a stable sol was obtained only in the presented sequence. In order to find the best aging time, the gel was aged for 12 hours and 1, 3, 7, and 14 days. Then, aged gels were dried in an oven and the as-dried gels were subsequently calcined in stagnant air at 823, 873, 923, 973, 1073, 1173, 1273, 1373, and 1473 K (550, 600, 650, 700, 800, 900, 1000, 1100, and 1200 °C) for 1 hour (heating rate of 3 °C/min), giving rise to the formation of gray powders.

B. Conventional Sol-Gel Approach ("Method B")

For comparison purposes, FHA nanopowders were also synthesized through the conventional alkoxide-based sol-gel approach. The details of synthesis steps in this technique can be seen in Figure 1(b). In summary, first, a P₂O₅ precursor was refluxed for 24 hours in a sealed container to obtain a clear solution. Moreover, pH of the mixture during dropwise addition of calcium precursor solution into the P-F mixture (adjusting the Ca/P ratio to 1.67) was carefully monitored and adjusted to 1 or less by adding HNO₃. In the higher pH values, precipitation occurred during addition of calcium precursor solution into the P-F mixture and stable sol was not formed.

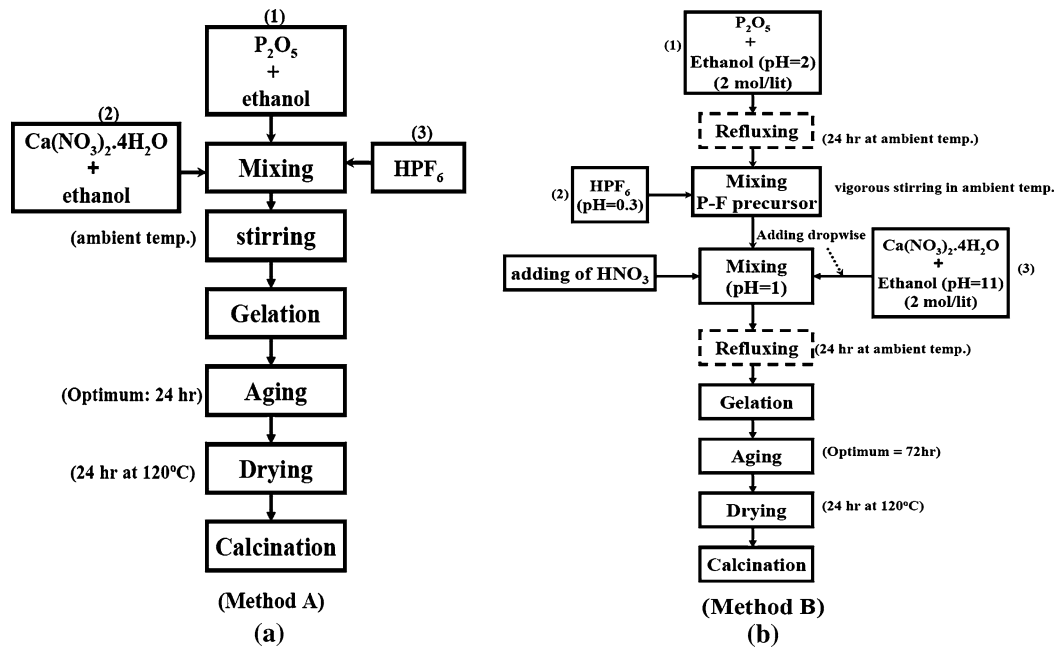


Fig. 1—Flowchart of FHA preparation through (a) the modified sol-gel route (method A) and (b) the conventional alkoxide-based sol-gel route (method B).

Table I. Designed Amounts of Precursors Dissolved in Initial Solution (Method A) and Observed Gelation Time for Each FHA Sample in Methods A and B

	FHA0 ($x = 0$)	FHA25 ($x = 0.5$)	FHA50 ($x = 1$)	FHA75 ($x = 1.5$)	FHA100 ($x = 2$)
Ca(NO ₃) ₂ ·4H ₂ O (gr)	7	7	7	7	7
P ₂ O ₅ (gr)	1.262	1.245	1.227	1.210	1.192
HPF ₆ (μL)	0	35.14	70.28	105.42	140.56
Gelation time (h) (method A)	24	23	20.5	18	15
Gelation time (h) (method B)	50	45	41	37	32

C. Structural Evaluation

Phase structure evaluation was carried out using the XRD technique (Philips X'Pert MPD Diffractometer, Royal Philips Electronics, Eindhoven, The Netherlands) using Ni-filtered CuK_α ($\lambda_{\text{CuK}\alpha} = 0.154186$ nm, radiation at 40 kV and 30 mA) over the 2θ range of 20 to 60 deg. The grain size of synthesized FHA samples was estimated with Scherer's formula:^[31]

$$t = \frac{0.89\lambda}{B \cos \theta} \quad [1]$$

where λ is the wavelength of the X-ray (nm), B is the full-width of the diffraction peak under consideration (rad) in the middle of its height considered after computer fit of the X-ray data using the Gaussian line shape, and θ is the Bragg's angle (deg). (002), (211), and (004) Miller's planes were used for the crystallite size determination of each sample, and the average was reported as crystallite size. The fraction of crystalline phase (X_c) was calculated by Eq. 2:^[32]

$$X_c = 1 - \frac{V_{112/300}}{I_{300}} \quad [2]$$

where I_{300} is the intensity of the (300) diffraction peak and $V_{112/300}$ is the intensity of the hollow between (112) and (300) reflections, which would completely disappear in amorphous samples. Reportedly,^[32] verification was made as follows:

$$B_{002} \sqrt[3]{X_c} \sim K \quad [3]$$

In this equation, K is a constant equal to 0.24 for very large numbers of different apatite powders, and B_{002} is the full-width at half-maximum (deg) of the (002) diffraction peak. The functional groups of obtained powders were analyzed by fourier transform infrared (FTIR) spectroscopy (Bomem MB 100, Hartman & Braun, Quebec, Canada) in a mid-IR spectrum range in the range of 400 to 4000 cm⁻¹. Transmission electron microscopy (TEM, Philips CM 200, Royal Philips Electronics, Eindhoven, The Netherlands) operating at accelerating voltage of 200 kV was used to study the morphology and particle size of the powder. An ion-meter (GLP 22, Crison, Barcelona, Spain) was also employed to determine real fluorine content of FHA powders. For doing this measurement, a specified amount of each FHA sample was dissolved in an acid

solution and then diluted. The fluorine content of this solution was analyzed using the pF-meter with a fluorine ion sensitive electrode (I.S.E. Electrode, Code: 9655, Crison). For evaluation of powder purity, element analysis was conducted with an inductively coupled plasma–optical emission spectroscope (ICP-OES: Jobin Yvon, Horiba Group) in a low resolution, high sensitivity mode to determine heavy metals as specified in ASTM F1185-88,^[33] rare earth, and other elements. Detected elements included Ag, Al, As, Ba, Cd, Ce, Co, Cr, Cs, Cu, Ga, Cd, Ge, Hg, Mg, Mn, Mo, Ni, Pb, Sn, Ti, W, and Zn. As-prepared gels were examined by differential thermal analysis and thermogravimetric analysis (DTA/TGA-Linseis Instruments L70/2171, Selb, Germany) in flowing air (20 mL/min) from ambient temperature to 1473 K (1200 °C) at a heating rate of 5 °C/min to monitor the weight loss and thermal behavior of the dried gels.

D. Coatings Preparation

For the dip-coating process, the preparation method of FHA sols was similar to the method described in Section A (Figure 1(a)). However, in order to prepare the sol for the dip-coating process, mixing of the solution was done in a fully-sealed beaker to prevent evaporation of the solvent (absolute ethanol) and gelation of the sol. After 24 hours of mixing, obtained sol was divided into two parts and these two parts were aged for 0 and 24 hours (in a sealed beaker) in order to evaluate the effect of aging time on the morphology and quality of the coating. FHA coatings were applied on the stainless steel 316L (SS) substrate *via* the dip-coating technique at ambient temperature.

Before starting the coating deposition, the SS substrates were abraded with silicon carbide (SiC) papers (grit range: 80 to 4000) and subsequently polished with 6-, 1-, and 0.05- μm polishing pad and ultrasonically washed with distilled water, alcohol, and acetone. After deposition of the coating, samples were dried at 393 K (120 °C) for 24 hours and then calcined at 873 K (600 °C) for 1 hour. Phase analysis and morphology of the coatings were studied by XRD and scanning electron microscopy (SEM: Philips XL 30, Royal Philips Electronics, Eindhoven, The Netherlands), respectively.

The designed degree of substitution of OH^{-1} by F^{-1} was indicated by the x value in the general formula of FHA ($\text{Ca}_{10}(\text{PO}_4)_6\text{OH}_{2-x}\text{F}_x$), where x values were selected equal to 0.0, 0.5, 1.0, 1.5, and 2. The subsequently obtained powders and coatings were named as FHA0, FHA25, FHA50, FHA75, and FHA100, respectively.

III. RESULTS AND DISCUSSION

A. Gelation Behavior of the Sol

In “method A,” after 15 minutes of stirring, the precursors were completely dissolved in the initial solution and a transparent sol formed. Upon continuation

of stirring, a change in viscosity was observed for all samples toward the end of the stirring period, but the viscosity increasing rate of the FHA100 sample was higher than the others and final gel was formed in a shorter time for the FHA100 sample. FHA0 and FHA25 sols showed the same behavior in terms of viscosity increasing rate and gelation kinetic during stirring time. It was observed that during stirring of the sol, the volume of the sol slowly decreased because of the gradual evaporation of the alcoholic solvent and sol became gradually more concentrated. At the final stage of stirring, gelation occurred and a very viscous and condensed phase appeared. The volume ratio of the obtained gel to initial sol was 1/12. The occurrence of gelation means that sufficient polymerization took place during stirring to form a semirigid structure.^[34] According to the observed gelation times for the various FHA sols prepared through method A (Table I), it is obvious that with increasing the amount of HPF_6 concentration in the initial FHA sols, the gelation took place faster and the viscosity increasing rate rose.

Gelation kinetic of the FHA sols prepared through method A was faster than the gelation kinetic of the FHA sols prepared through “method B,” presumably as a result of a faster polymerization. In both methods, it seems that increasing the concentration of fluorine ions in the sol reduced the gelation time and improved the gelation behavior. After drying, the gel was transformed into a highly porous and amorphous white structure. A reduction in the gelation time of FHA sols, prepared through an alkoxide-based sol-gel technique, from 6 to 2 months was previously reported, when the HPF_6/Ca ratio in the sol increased from 0 (HA) to 3/90 (FA).^[24]

B. DSC/DTA/TGA

The results of TGA combined with differential scanning calorimetry (DSC) and DTA, conducted on the as-dried gel (24 hours of aging) of the FHA100 sample synthesized through method A, can be seen in Figure 2.

Three weight loss steps are distinguishable in the TGA diagram, and the corresponding temperature regions of 313 to 456 K (40 to 183 °C), 456 to 558 K (183 to 285 °C), and 558 to 800 K (285 to 527 °C) could be easily identified. In the first step, a small weight loss of about 6.3 wt pct was detected, where two small endothermic peaks could be observed at about 403 and 448 K (130 and 175 °C); this weight loss seems to correspond to the evaporation of volatile components such as ethanol and adsorbed water,^[35] which was probably promoted by the distraction effect of ethanol.^[36] In the second stage, a sharp weight loss of about 18.9 wt pct combined with a sharp exothermic peak at 543 K (270 °C) corresponded to the crystallization of apatite.^[35,37] In the third stage, a sharp weight loss of 17.2 wt pct combined with a small endothermic peak at 783 K (510 °C) confirmed the removal of residuals such as structural water and decomposition of the nitrate group.^[35,37] There is another very small endothermic peak at 493 K (220 °C), but the origin of this peak is not clear. However, this unknown endothermic peak was

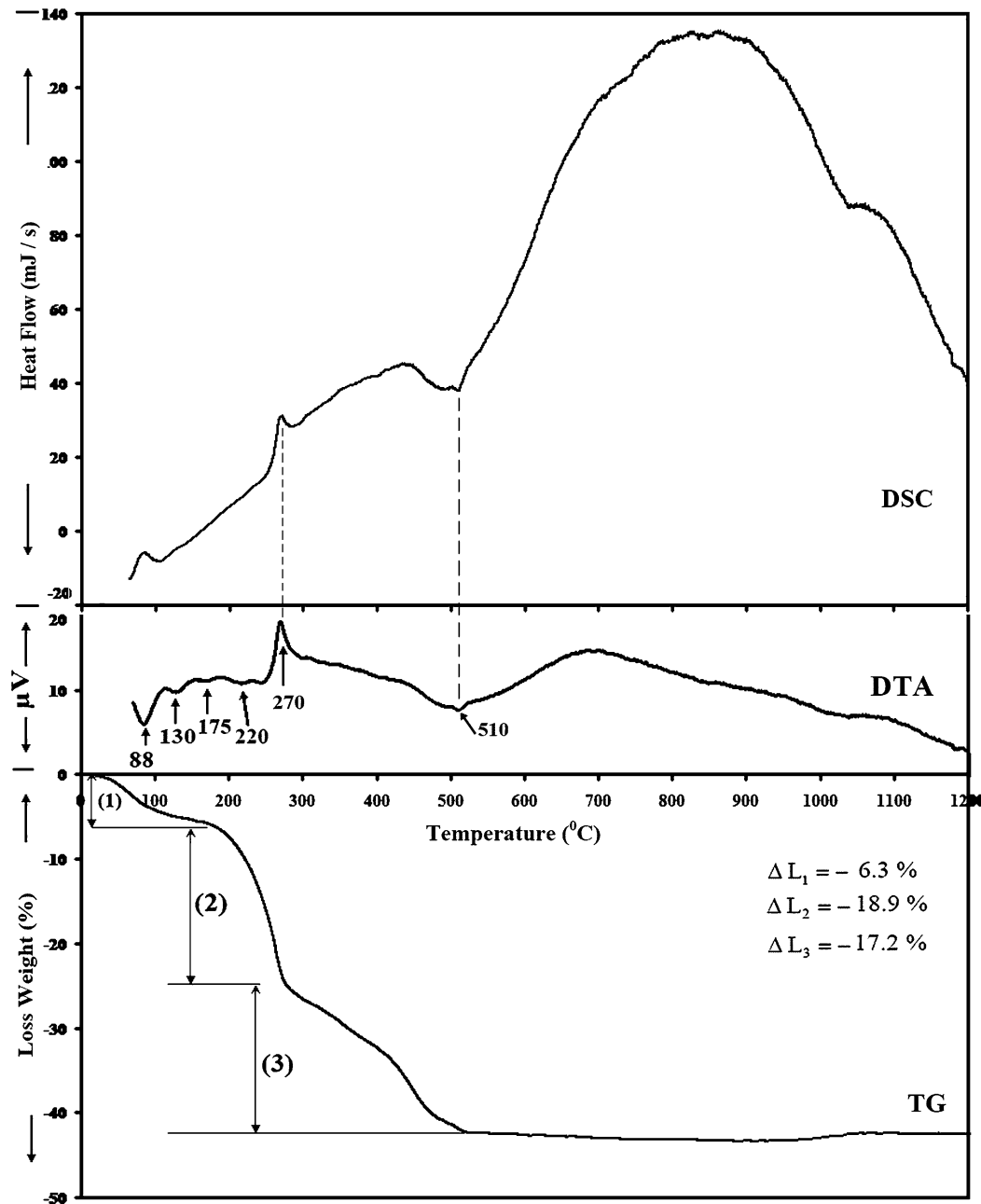


Fig. 2—DSC, DTA, and TGA curves of the as-dried FHA100 gel obtained through method A after 24 h of aging.

probably caused by removal of other chemical groups in the precursors. Obviously, there are no other considerable weight loss stages above 800 K (527 °C), indicating that the precursors generated a stable phase after calcination at temperatures above 800 K (527 °C).

C. Aging Time Optimization

X-ray diffraction (XRD) patterns of FHA100 nanopowders, at various aging times, synthesized through method A, are shown in Figure 3(a) in comparison with the as-dried nonaged gel. In the as-dried gel X-ray pattern, in addition to a strong amorphous background, weak and broad characteristic peaks of $\text{Ca}_2\text{P}_2\text{O}_7$,

$\text{Ca}(\text{NO}_3)_2 \cdot 2\text{H}_2\text{O}$, and $\text{Ca}(\text{NO}_3)_2$ phases, and some other unknown phases, were identified. These impurity phases generally are identifiable in short time aged gels and disappear after calcination because of the occurrence of thermally activated reactions.^[38] This unknown phase has been attributed to transient organic crystals,^[24] since the position and intensity of these unknown phase reflections did not have any match with JCDP cards. There is no crystalline FA phase observed in the as-dried state of the gel, confirming that the FA remains amorphous. Obviously, no characteristic peaks of CaF_2 could be identified in the as-dried gel. This means that F^{-1} ions released from HPF_6 dissociation because of hydrolysis and alcoholizing during mixing completely reacted with

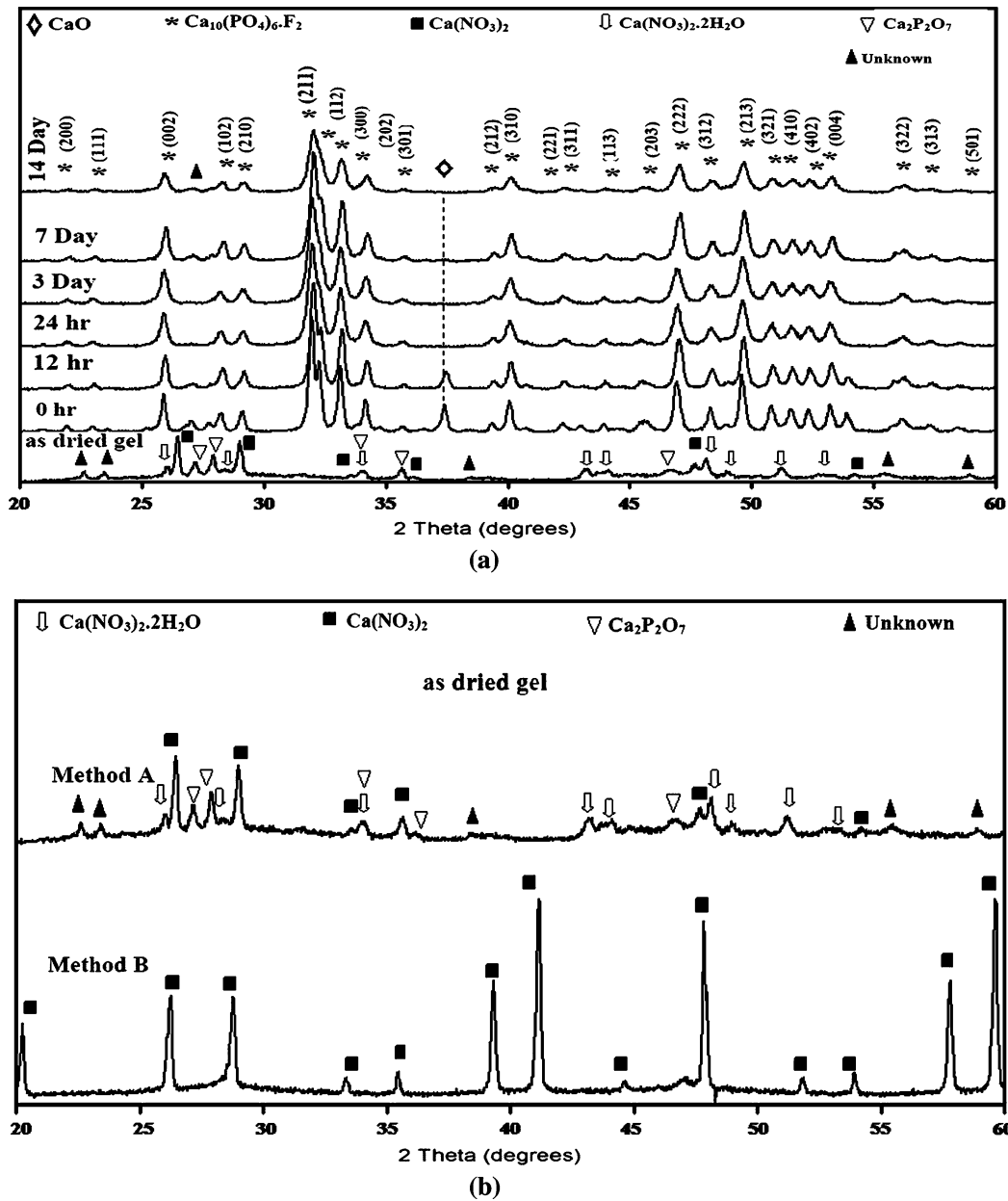


Fig. 3—XRD patterns of (a) synthesized FHA100 nanopowders (method A), calcined at 873 K (600 °C) for 1 h, after various aging times compared to the as-dried gel without aging. (b) As-dried FHA100 gels synthesized through methods A and B without aging.

P-O and PO_3^{-4} groups and, subsequently, entered into the amorphous calcium phosphate phase. As a direct result of these phenomena, no F^{-1} ions reacted with residual Ca^{++} in the solution to form CaF_2 . This simple observation confirmed that in method A, the behavior of F^{-1} ions during sol-gel reactions could not be explained by the mechanisms suggested for an alkoxide-based sol-gel technique,^[24,25] based on the formation of nanocrystalline CaF_2 at the beginning of the mixing step. Further research is required in order to clarify the exact mechanism of FA formation and to also explain the specified reactions occurring in this modified sol-gel technique. This will be the scope of our future work.

The calcium nitrate and $\text{Ca}_2\text{P}_2\text{O}_7$ impurity phases remained in the as-dried gel because of the incomplete

reaction between the precursors during the mixing step and disappeared after calcination at 873 K (600 °C). Strong amorphous background and also weak and broad peaks of the crystalline phases in the pattern of as-dried gel obtained from method A (Figure 3(b)) illustrated that as-dried gel mainly consists of amorphous apatite phase, which was produced as a result of reactions during mixing and transforming of the sol into the gel. During the aging step, the gel was completely stable and no precipitation occurred even at higher aging times. Visual observation confirmed that the gel remained light translucent during aging regardless of the time.

In the calcined FHA100 nanopowder with 0 and 12 hours of aging time, in addition to the crystallized

FA phase, impurity phases such as the unknown phase ($2\theta = 27.15$ deg), $\text{Ca}_2\text{P}_2\text{O}_7$ ($2\theta = 27.91$ deg), and CaO ($2\theta = 37.45$ deg) still could be found in the powders. Formation of CaO after calcination confirmed the presence of unreacted calcium phases in the composition of the 12-hour aged gels. When the aging time increased up to 24 and 72 hours, the FA peaks' sharpness and intensity, which could, respectively, show the crystallinity and concentration of apatite,^[38] were slowly increased. By further increasing the aging time up to 1 and 2 weeks, a peak assigned to the unknown phase appeared again in the patterns, but no decomposition of FA to other calcium phosphate phases such as TCP, TTCP, and CaO was observed. Clearly, the lowest FA peak intensity and peak sharpness belong to the FA produced after 14 days of aging. Based on these results, 24 hours is the optimum aging time for the FA powders synthesized through method A compared to the 72 hours for method B.

XRD patterns of the as-dried gels (without aging), synthesized through methods A and B, can be seen in Figure 3(b). In terms of phase composition, an obvious difference between these two dried gels is notable. Sharp peaks of $\text{Ca}(\text{NO}_3)_2$ as initial material residue with low amorphous background can be seen in the pattern attributed to method B, and the pattern with stronger amorphous background (highest amount of amorphous phase) as well as weak and broad peaks of the crystalline phases belonged to the gel, formed in method A. Clearly, in the modified sol-gel technique, reactions between the calcium precursor and other reactants, which occurred during the mixing step, were significantly improved compared to the conventional technique. A higher amount of Ca^{++} in method A entered into the amorphous calcium phosphate phase after gelation instead of remaining in the final product as a residual calcium nitrate phase. Therefore, it is plausible to claim that sol-gel technique modification easily improved polymerization and the gelation kinetic of the initial sol in method A. Based on the crystallite size calculations (Eq. [1]) for the calcined FA at 873 K (600 °C) after various aging times, the crystallite sizes were calculated to be 19.7(1), 22(1), 25.3(2), 34(0.5), and 52.7(2) nm for 0, 12, 24, 72, and 168 hours of aging, respectively.

To explain the increase in crystallite size by increasing the gelation time, it is worth mentioning that, in the gelation step of the sol-gel process, polymerization reactions occurred to form cross-linking of the molecules at the drying step and making up of the skeletal structure. Available pores in the polymeric skeletal structure provided suitable spaces for ceramic particles. As a result of skeletal structure formation, more M-O-M bands would be created in the structure, which would make it stiffer.^[34] In this system, the M character in M-O-M bands is phosphorous atoms, which were connected together through oxygen bands in the cross-link network. It was previously shown that, as the aging time increased, the cross-link structure also increased, and increasing the cross-link structure caused a rise in the final size of the apatite crystallite;^[39] this correlation could play an important role in the application of

apatite in the biomedical field, for example, in nonviral gene delivery.

D. Structural Characterization

The phase composition of sol-gel-derived FHA0, FHA25, FHA50, FHA75, and FHA100 nanopowders, calcined at 873 K (600 °C) for 1 hour, was analyzed by XRD, as shown in Figure 4. According to the patterns, for all samples with different degrees of fluoridation, a single-phase apatite was formed and no other peaks except characteristic apatite peaks could be observed. Moreover, X-ray patterns exhibited almost identical patterns with high crystallinity. The (211) and (112) peaks of the fluorinated samples merge due to the fluorination, especially when the degree of fluorination is higher than 25 pct. This is in agreement with the observations made by Murugan *et al.*^[5] A closer examination of the apatite peaks revealed a gradual peak shift in the main diffraction peaks in FHA samples toward higher degrees with increasing the fluoridation level, which was in good agreement with a previous study.^[29] Considering the phosphate tetrahedral group, whose members are not connected to each other and oriented toward calcium ions along the *a*-axis of the apatite crystallographic structure, fluorine and hydroxyl groups as electronegative ions are placed perpendicularly to Ca^{2+} ions along the *c*-axis.^[40] Substitution of OH^- groups with F^- ions in the apatite structure did not change the hexagonal crystallographic structure of the apatite.^[41] Nonetheless, the different sizes of the ions

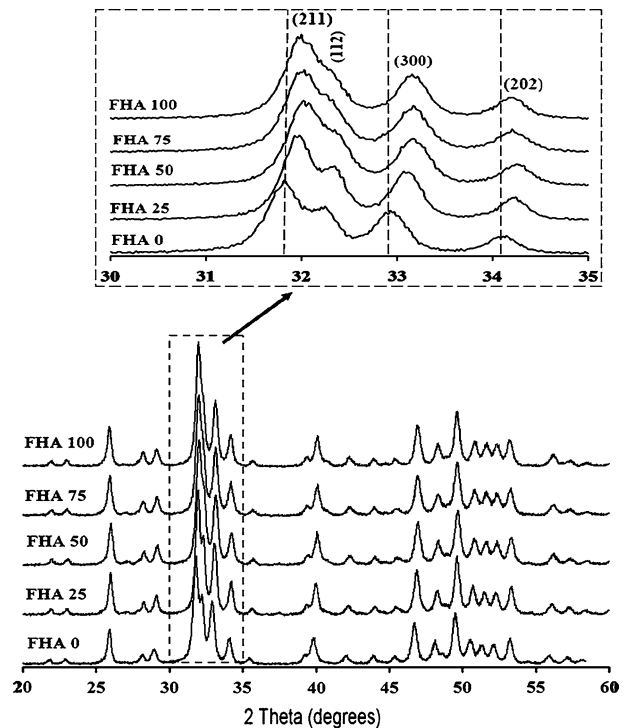


Fig. 4—XRD patterns of sol-gel derived FHA0, FHA25, FHA50, FHA75, and FHA100 nanopowders (method A), after 24 h of aging and calcination at 873 K (600 °C) for 1 h, show only characteristic peaks of apatite.

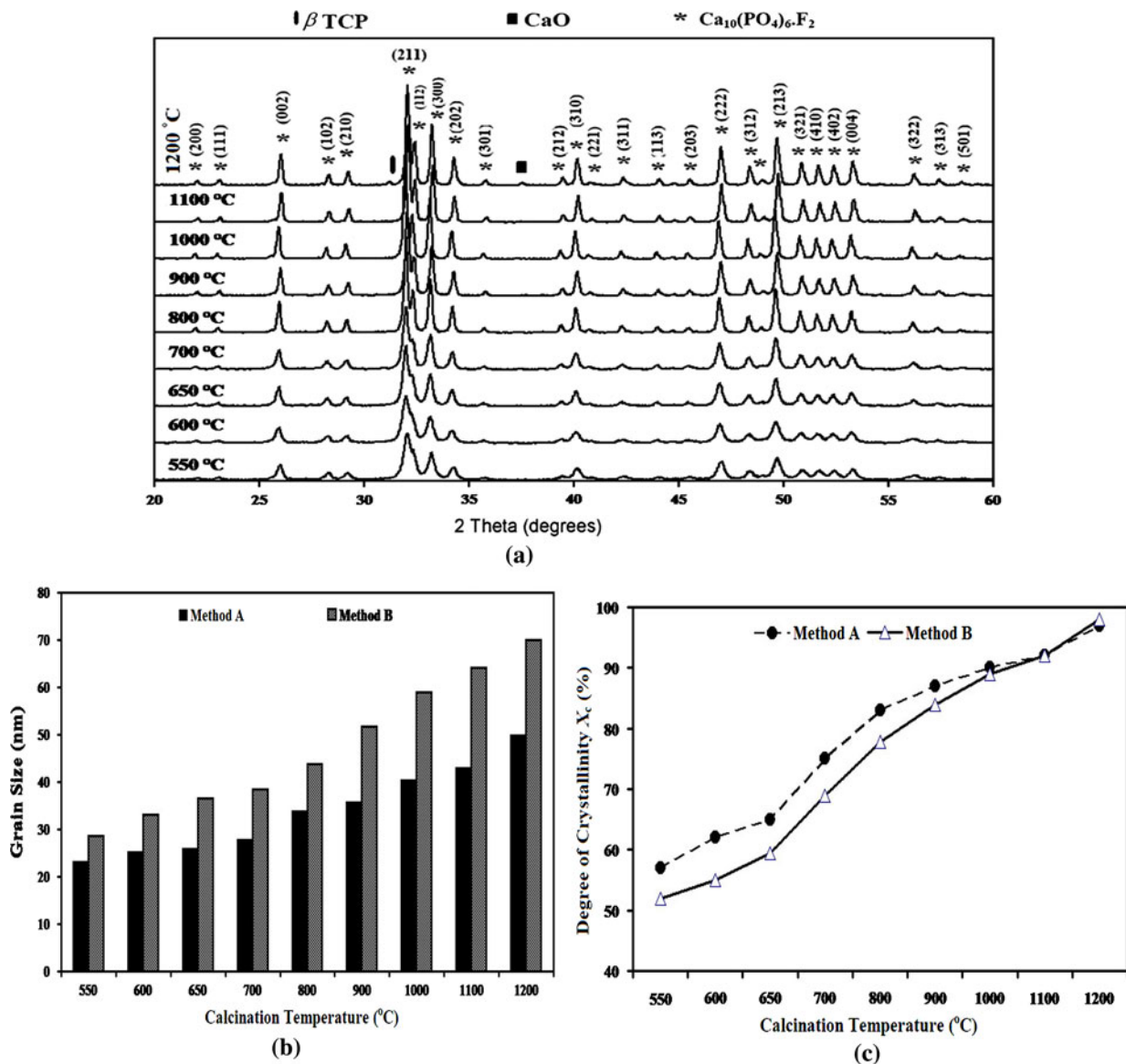


Fig. 5—(a) XRD patterns (method A), (b) crystallite sizes, and (c) crystallinity of FHA100 nanopowders, after 24 h of aging and 1 h calcination at different temperatures.

cause a contraction of the a -axis without any significant changes to the c -axis.^[29] As was previously reported, the slight shift of the apatite characteristic peaks was attributed to this contraction in the a -axis length of the hexagonal apatite's crystal lattice due to lower ionic radii of F^{-1} (1.32 Å) than OH^{-1} (1.68 Å), which introduced distortion in the lattice. The peak intensity increased continuously with increasing F^{-1} content of the FHA powders, confirming a rise in the crystallinity of the powders.^[29] Previous work showed that incorporation of fluorine ions into the apatite structure enhances the development of the apatite phase, letting the FHA nanopowders have the stronger XRD intensities of apatite compared to the pure HA nanopowders.^[25] This point was also mentioned by Wang *et al.* for FHA synthesized through the electrochemical deposition technique.^[28]

Figure 5(a) shows the effect of the as-dried FHA100 powder calcination temperature on the formation and phase composition of the nanocrystalline fluorapatite (FA) powder (method A). XRD peaks were indexed on the basis of the hexagonal crystallographic system of the space group $p6_3/M$.^[42] The d spacing of synthesized FHA100 powder (method A), calcined at 873 K (600 °C) after 24 hours of aging, was compared with the standard card of FA (JCDP 15-0876),^[42] and there was a good match with the standard both in terms of relative intensity and the position of the peaks, as can be seen in Table II. This finding could be evidence that fluoride ions entered completely into the crystallographic structure of apatite in the FHA100 sample. At 823 K (550 °C), the presence of both broad and weak peaks was an indication of FA phase formation, and both the broad envelope shape and weak intensity of

Table II. *d* Spacing of FHA100 Nanopowder Prepared by Method A, after 24 Hours of Aging and Calcination at 873 K (600 °C), in Comparison with JCDP Card (FA,15-0876)

<i>d</i> (nm)		Intensity		
Experimental	JCPDC (15-0876)	Experimental	JCPDC (15-0876)	(<i>hkl</i>)
0.3440	0.3442	37	40	002
0.3064	0.3067	12.4	18	210
0.2800	0.2800	100	100	211
0.2771	0.27720	53.5	55	112
0.2702	0.27020	54.1	60	300
0.2626	0.2624	24.4	30	202
0.2249	0.2250	19	20	310
0.1935	0.1937	28.9	25	222
0.1884	0.1884	11.6	14	312
0.1837	0.1837	29.9	30	213
0.1722	0.1722	13.5	16	004

peaks with strong amorphous background revealed that the newly formed FA phase was poorly crystallized. Increasing the calcination temperature up to 1473 K (1200 °C) resulted in a further increase of crystalline order of the apatite phase and further sharpening of the principal diffraction peaks. Clearly, FA remained stable up to 1373 K (1100 °C), since no additional crystalline phases such as CaO, CaF₂, and TCP were observed in the patterns. Only after calcination at 1473 K (1200 °C), β-TCP, and CaO phases appeared in the XRD pattern as a result of apatite decomposition at this temperature. However, the decomposition temperature of FA strongly depends on the synthesis techniques, which could have direct effects on the characteristics of the product. As a result, different decomposition temperatures have been reported for FA in the literature. The thermal decomposition temperature of sol-gel derived FA nanopowder, reported in one study, was 1173 K (900 °C), where inorganic chemical compounds were used as starting materials.^[26] In another report,^[24] the synthesized FA powder, using similar starting materials compared to the present work, but throughout an alkoxide-based sol-gel technique (comparable to method B which was used in this study), was stable at 973 K (700 °C). Bianco *et al.*^[9] reported the successful production of needlelike FHA50 *via* the precipitation method, which was thermally stable up to 1573 K (1300 °C). Also, it has been reported that HA decomposed within the temperature range of 873 to 1073 K (600 to 800 °C).^[43]

Higher decomposition temperature of FA compared to HA could be explained by considering the crystal structure of apatite. The hydrogen (H⁺) ions of HA were arranged in atomic interstices neighboring the oxygen ions (O⁻²) along the *c*-axis of apatite structure, forming OH⁻¹ groups, and were oriented randomly, which conferred a certain degree of disorder to the crystal structure of HA. Once the OH⁻¹ groups were partially substituted by the F⁻¹ ions, the existing hydrogen ions of the OH⁻¹ groups were bound to the nearby F⁻¹ ions because of the higher affinity of the F⁻¹ ions compared to the oxygen ions, producing a quite

well-ordered apatite structure, which caused a rise in the resistance of the material to thermal decomposition. Therefore, when F⁻¹ ions substituted the OH⁻¹ groups in the HA matrix, thermal decomposition resistance of the apatite ceramics was achieved.^[2,8,9]

A comparison was made between crystallite sizes of FHA100 nanopowders synthesized through these two different methods at different calcination temperatures in Figure 5(b). As can be deduced from this bar chart, when the calcination temperature increased, the crystallite size of the synthesized FHA100 nanopowder followed an upward trend. The increasing slope as well as the amount of calculated crystallite size for synthesized FHA100 nanopowder in method B was considerably higher than those parameters for the synthesized FHA100 nanopowders in method A. In fact, as a result of polymeric chain extraction, which was caused by firing of the amorphous powder in drying step, there is no obstacle for grain growth, which is why increasing the size of nanoparticles was observed as a result of a rise in the calcination temperature.

Also, Figure 5(c) shows an upward trend in the amount of calculated crystallinity for synthesized FHA100 in both methods, when the calcination temperature increased. Obviously, for calcination temperatures lower than 1273 K (1000 °C), the crystallinity of the nanopowders synthesized through method A is higher than that for the samples prepared through method B, but for the calcination temperature of 1273 K (1000 °C) or higher, the amounts of calculated crystallinity for both samples were similar. Lopatin *et al.*^[44] explained that when apatite phase formed during the calcination step, the cross-link structure, which was generated after completing the polymerization and gelation, must be rearranged to form the characteristic apatite crystallographic structure. As a result of this structural rearrangement, which is not well understood, calcium and fluorine ions arranged in the channels formed between the columns of the phosphate ions probably by a diffusion control mechanism. In fact, the presence of less cross-linked in the dried gel structure makes the formation and crystallization of apatite phase much easier. Based on this mechanism, presumably, the amount of cross-linked formed in the structure during the gelation and drying of the gel in the alkoxide-based sol-gel technique (method B) is higher than the amount of cross-linked formed in method A. As a result, the crystallization of the FA from the dried gel synthesized in method A is much easier, and therefore, the crystallinity of the FA powder formed in method A is higher than that in method B (Figure 5(c)). It seems that because of the very fast diffusion rate of atoms and ions at temperatures higher than 1273 K (1000 °C), during the rearrangement process, the cross-linked structure could not restrict the crystallization of FA from the dried gel, synthesized *via* method B; as a result, the amounts of FA crystallinity in both methods showed similar values at calcination temperatures above 1273 K (1000 °C). Moreover, since increasing the cross-linked structure caused an increase in the crystallite size of the synthesized apatite powder,^[39] the higher crystallite

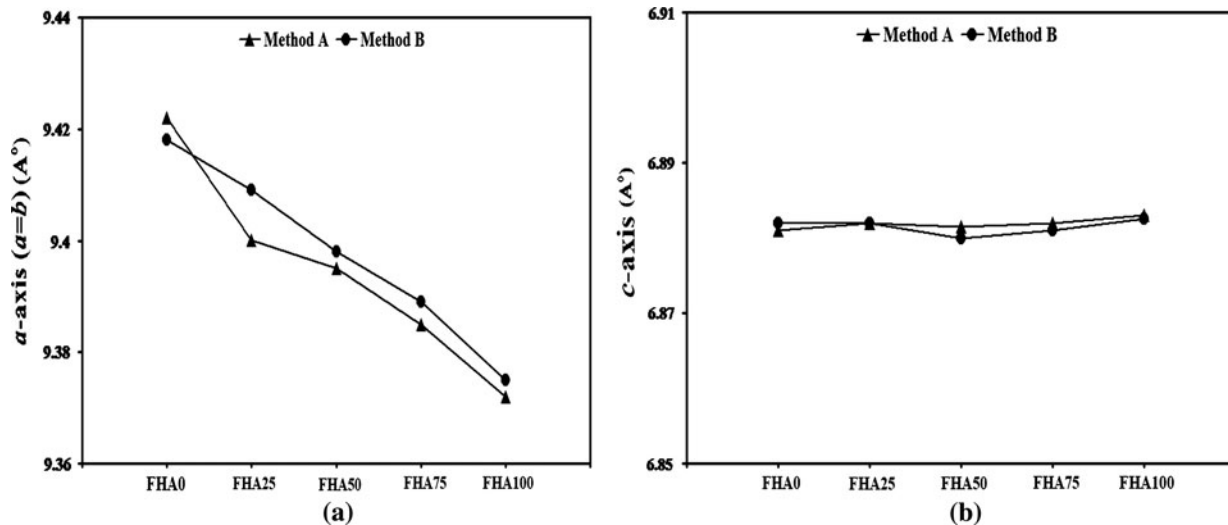


Fig. 6—Trend of calculated lattice parameters (a) a -axis and (b) c -axis of FHA0, FHA25, FHA50, FHA75, and FHA100 nanopowders synthesized through methods A and B, calcined at 873 K (600 °C) for 1 h after 24 h of aging.

size of the FA synthesized through method B compared to method A (Figure 5(b)) could also be easily deduced.^[39]

The amounts of sol-gel prepared FHA nanopowder lattice parameters (calcined at 873 K (600 °C) for 1 hour, after 24 hours of aging), calculated using XRD data, can be seen in Figure 6(a) (a -axis) and Figure 6(b) (c -axis). These calculated lattice parameters for FHA powders could be used to estimate the degree of FHA nanopowder fluoridation synthesized through methods A and B. Obviously, as the concentration of incorporated F^{-1} into the apatite structure increased, the a -axis decreased steadily, but the c -axis remained almost unchanged. For method A products, there was a significant decrease in the a -axis from 9.422 Å for FHA0 down to 9.372 Å for FHA100. For FHA nanopowders synthesized through method B, the corresponding values were 9.418 Å for FHA0 and 9.375 Å for FHA100. Similar values of the c -axis (average: ~6.8819 Å for method A and 6.8815 Å for method B) for all samples were observed (constant trend in Figure 6(b)).

These results correspond with the slight shift of characteristic peaks of apatite in Figure 4. The fluorine-hydroxyl substitution occurred in channels located along the c -axis in the apatite structure, and because of the lower ionic radii of F^{-1} compared to OH^{-1} , which was mentioned before, there is no change in cell parameter dimension in the c -axis direction,^[2,9,21] but a contraction occurred in the a -axis direction as the degree of fluorination increased. Therefore, the amount of contraction in the a -axis lattice parameters is proportional to the amount of fluorine ions incorporated into the apatite structure. Since the amount of a lattice parameter calculated for each FHA sample in method A is less than method B, expectedly, real amounts of incorporated F^{-1} ions into the apatite structure (real degree of fluoridation) through method A are higher than those through method B. This point will be quantitatively discussed further in section F.

Based on the employed synthesis techniques and probable substitution of other ions into the apatite structure in addition to F^{-1} , different values for the lattice constant of FHA could be found in the literature. The lattice constant of pure FHA0 generally corresponded to the data that was previously reported,^[45] $a = b = 9.432$ Å and $c = 6.881$ Å; but the a value was a bit smaller. Moreover, a and c values of FHA0 compounds were in good agreement with those of $a = 9.4155$ Å and $c = 6.881$ Å,^[46] $a = 9.422$ Å and $c = 6.884$ Å,^[9] $a = 9.419$ Å and $c = 6.884$ Å,^[28] $a = 9.418$ Å and $c = 6.884$ Å,^[47] and $a = 9.414$ Å and $c = 6.881$ Å.^[48] The measured lattice constant values of FHA100 were in excellent agreement with the other reports: $a = b = 9.3716$ Å and $c = 6.884$ Å,^[46] $a = b = 9.370$ Å and $c = 6.882$ Å,^[48] and $a = b = 9.364$ Å and $c = 6.884$ Å.^[42] The lattice constant of the $Ca_{10}(PO_4)_6(OH)$, synthesized via the precipitation method,^[9] was equal to $a = b = 9.39$ Å and $c = 6.882$ Å, which are close to the lattice constant values for FHA50 in the present work.

E. Fourier Transform Infrared Analysis

FTIR spectra of the obtained FHA nanopowders, prepared through method A after calcination at 873 K (600 °C) for 1 and 24 hours of aging, are shown in Figure 7. All patterns were the characteristic patterns of carbonated apatite, as discussed in another report.^[48] At each spectrum, no other peaks that would come from extraneous substitution of functional groups were observed, and each of the synthesized nanopowders was characteristic of apatite compounds. With regard to the carbonates (CO_3^{2-}), the band centered at 869 cm^{-1} for ν_2 and a doublet at 1470 and 1429 cm^{-1} for ν_3 were visible in the spectra. These peaks confirmed that the FHA contained some CO_3^{2-} groups in PO_4^{3-} sites of apatite lattice (B-type substitution).^[49] Reportedly, this kind of apatite is similar to biological apatite and could be more suitable for bone scaffolding purposes.^[49]

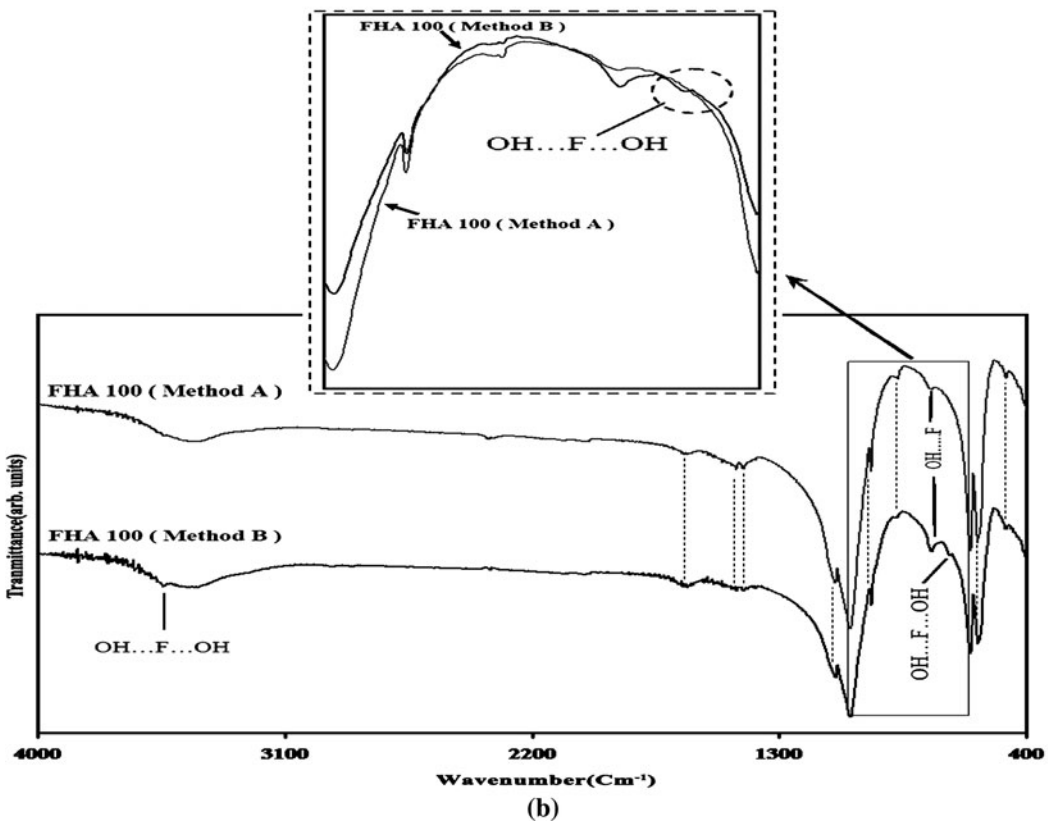
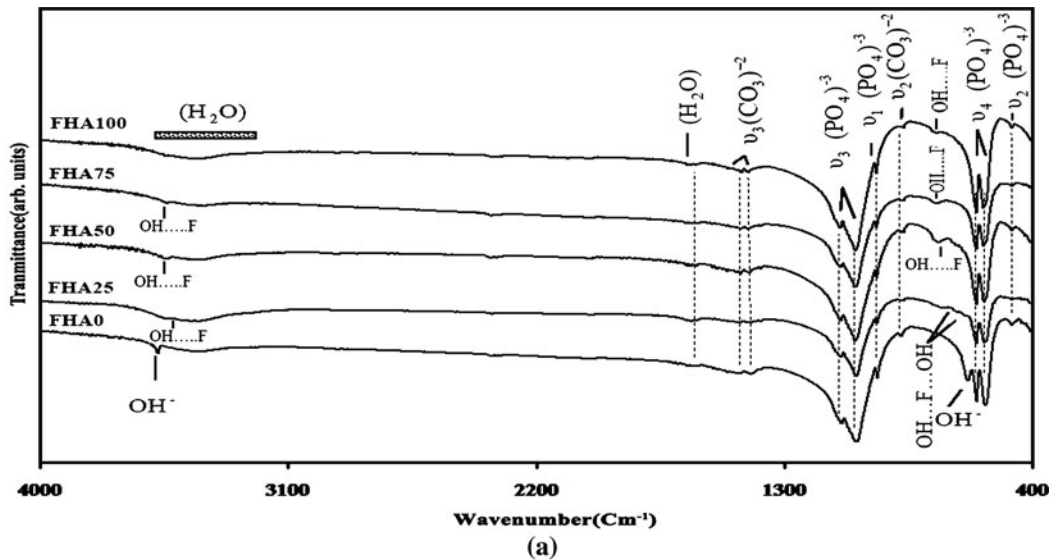


Fig. 7—FTIR spectra of (a) sol-gel synthesized FHA nanopowders, calcined at 873 K (600 °C) for 1 h after 24 h of aging, with 0, 25, 50, 75, and 100 pct degree of fluoridation (method A) and (b) FHA100 compounds synthesized through methods A and B.

The characteristic peaks of PO_4^{3-} tetrahedral groups, which had four distinct asymmetrical stretching vibration modes, namely, ν_1 , ν_2 , ν_3 , and ν_4 , appeared in the broad spectrum. The ν_1 and ν_2 vibration peaks were observed at 960 cm^{-1} (P-O stretching ν_1) and at 470 cm^{-1} (O-P-O bending ν_2), respectively. As a major peak of phosphate group, the P-O stretching ν_3 vibration mode was visible in the region between 1100 and 1000 cm^{-1} (two noticeable splittings at 1035 and 1091 cm^{-1}), which was the most intensified peak among

the phosphate vibration modes. The band between 612 and 560 cm^{-1} showed the ν_4 vibration mode of the phosphate group, which occupied two sites in the crystal lattice, each at 605 (O-P-O bending ν_4) and 576 cm^{-1} (O-P-O antisymmetric bending ν_4). Two distinguishable splittings of ν_4 vibrations indicated the low site symmetry of molecules, as two peaks confirmed the presence of more than one distinction site for the phosphate group in apatite lattice.^[50] Increasing the fluorine content of the FHA samples caused an increase in the resolution of

the ν_3 vibration mode of the phosphate group and a change in the relative intensities of the ν_4 vibration mode of the PO_4^{3-} tetrahedral group. Two bands relating to vibration of the adsorbed water in apatite lattice could be noticed as a broad peak between 3690 and 3200 cm^{-1} (stretching frequency) and another widened band at 1645 cm^{-1} (bending mode).^[49,51] In the spectrum of the FHA0 sample, bands corresponding to the stretching and vibrational mode of structural hydroxyl groups at 3570 and 633 cm^{-1} ,^[13] respectively, were evidenced, suggesting fluoride substitution for OH^{-1} groups for the other four samples. In the spectrums of fluoridated samples, the intensity of these two bands decreased and these two bands disappeared, which was indicative of the substitution of F^{-1} for OH^{-1} . This effect is because an additional OH-F stretching band appeared at a lower frequency when the OH^{-1} was partially replaced by F^{-1} .^[28,29] From the strength of the hydrogen bonding point of view, the 3570 and 633 cm^{-1} vibrations are attributed to weak hydrogen bonding and stronger hydrogen bonding, respectively. It is worth mentioning that these two vibrations in the spectrum of the FHA0 sample were due to OH^{-1} immersed in an infinite chain of OH^{-1} , but this chain was interrupted by F^{-1} in the other four compounds since F^{-1} incorporated into the apatite lattice.

In the spectrum of the FHA25 sample, the band at 3530 was attributed to $\text{OH}\dots\text{F}$ and the bands at 713 as well as 659 cm^{-1} were assigned to the $\text{OH}\dots\text{F}\dots\text{OH}$ groups. Also, the bands at 744 and 3533 cm^{-1} in the spectrum of the FHA50 sample, 747 and 3536 cm^{-1} in the FHA75 spectrum, and, ultimately, 740 cm^{-1} in the spectrum of the FHA100 sample could be ascribed to the configuration FFOHFF , in which the single OH^{-} group could be between two orientations, $\dots\text{FOHF}\dots$ or $\dots\text{FHOF}\dots$ and may switch from the one to the other with a comparatively low energy.^[52] Based on the discussed results, as the fluoride ion content in the apatite lattice increased, the bands assigned to the $\text{F}\dots\text{OH}$ appeared and the bands assigned to the $\text{OH}\dots\text{F}\dots\text{OH}$ and structural OH^{-1} disappeared. Hydroxyl bands disappeared in the spectrum of fluorine substituted HA, which is why some researchers have neglected the existence of hydroxyl groups for mineral bone,^[53] while others subscribe to the view that in poor crystalline apatite, hydroxyl groups are simply not resolved.^[54] The results of the present study indicate that there was enough coupling to the fluoride to mask the characteristic hydroxyl band. There is also no evidence of bands that could be attributed to the $\text{OH}\dots\text{F}\dots\text{HO}$ groups in all spectra.^[52,55]

The FTIR spectra of the FHA100 samples, which were synthesized through methods A and B, were compared with each other in Figure 7(b). It is clear that the band, attributed to the $\text{OH}\dots\text{F}\dots\text{OH}$ group, could be easily detected in the spectrum of the FHA100 compound, synthesized through method B. It seems that the OH^{-1} chains in the FHA100 sample, synthesized through method B, were not completely rich in F^{-1} ions. In general, H, F apatite chains had $\dots\text{FHO}(\text{OH})n\text{HO}:\text{OH}(\text{OH})n\text{OHF}\dots$ configuration, where n depends on the OH^{-} and F^{-} ratio within the apatite. The term

n decreased with increasing F^{-1} ion content, and there was a $\dots\text{FHOHO}:\text{OHOHF}\dots$ configuration for $n = 0$: With further increase of F^{-1} vs OH^{-1} ion content in apatite, the chain reduces the number of OH^{-1} ions until the formation of $\dots\text{FHO}:\text{OHF}\dots$ and $\dots\text{FOHF}\dots$ chain configuration.^[48] Therefore, based on the presence of the band attributed to the $\text{OH}\dots\text{F}\dots\text{OH}$ group in the FAH100 compound (method B), it could be concluded that incorporation of the F^{-1} ions into the FHA100 apatite structure partially occurred during the alkoxide-based sol-gel technique (method B). This conclusion is in a good agreement with the judgment, which was made based on the a lattice parameter calculation (Figure 6) regarding to the lower fluorine ion incorporation into the apatite structure in method B compared to method A for each FHA sample.

Apatite containing both carbonate and fluorine ions has this potential to be used as bone graft material for orthopaedic and dental applications.^[56,57] In an *in-vivo* study by Kazimiroff *et al.* autoradiographic data showed a higher level of osteoblastic activity at the interface of bone/carbonated FA compared to the bone/HA interface.^[56] Another report published by Sakae *et al.*^[57] comparing the *in-vivo* performance of HA, carbonated hydroxyapatite (CHA), and carbonated fluorapatite (CFA) implanted in dog mandible, showed that CFA induced faster bone remodeling, and a more completely formed Haversian system was obtained with CFA compared to HA or CHA.^[58] Moreover, *in-vitro* study by Sakae *et al.* confirmed a lower number of resorption pits in CFA compared to HA and CHA.^[58,59]

F. ICP/OES and pF-Meter Analyses

Figure 8 shows the fluorine content (in terms of F/Ca) in FHA0, FHA25, FHA50, FHA75, and FHA100 nanopowders, calcined at 873 K ($600\text{ }^\circ\text{C}$) for 1 hour after 24 hours of aging, obtained by the pF meter with a

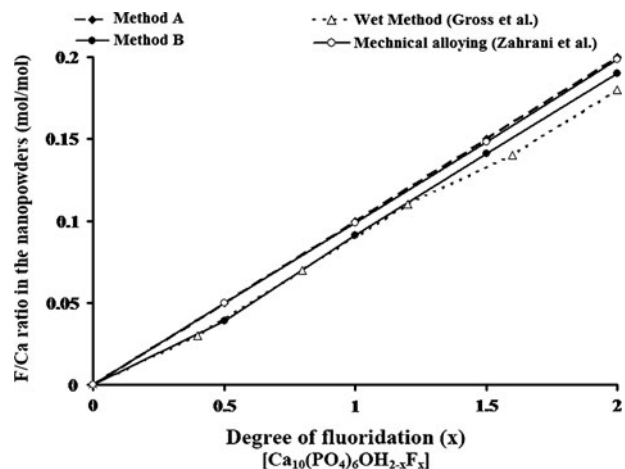


Fig. 8—Fluorine content of sol-gel derived FHA0 ($x = 0$), FHA25 ($x = 0.5$), FHA50 ($x = 1$), FHA75 ($x = 1.5$), and FHA100 ($x = 2$) nanopowders, calcined at 873 K ($600\text{ }^\circ\text{C}$) for 1 h after 24 h of aging in comparison with the results of other studies, Gross *et al.*^[59] and Zahrani *et al.*^[29].

fluorine ion sensitive electrode as a function of theoretical degree of fluoridation in comparison with the results reported for the wet^[59] and mechanical alloying process. Synthesis of FHA *via* the mechanical alloying technique was extensively discussed in our previous works; however, the results of fluorine content evaluation of the nanocrystalline products *via* the mechanical alloying technique were not presented. Therefore, in order to make a comparison between the sol-gel and mechanical alloying techniques in the production of FHA nanocrystalline powders in terms of fluorine ion incorporation efficiency into the structure, the fluorine contents of FHA nanocrystalline powders synthesized in our previous works^[29,48,60] were added into the current article and compared with the results obtained for the sol-gel derived nanopowders.

In Figure 8, the curves have the same trend, and in all techniques, fluorine content increased by increasing the theoretical degree of fluoridation. Based on these graphs, in method A, designed amounts of F^{-1} ions were incorporated into the FHA structure and the theoretical degree of fluorination is equal to the real degree of fluoridation for all FHA compounds, which is comparable with the results of the mechanical alloying method. However, in method B, all designed amounts of F^{-1} ions did not completely incorporate into the apatite lattice. However, for degrees of fluoridation (x) higher than 1, the performance of method B was better than that of the wet method^[59] in terms of successful incorporation of fluorine ion into the apatite structure. These quantitative measurements are in excellent correlation with the results of FTIR analysis (Figure 7(b)) and lattice parameters calculation (Figure 6(a)). Moreover, the F/Ca ratio in the sol-gel derived FHA nanopowders (method A) is higher than those reported by Gross *et al.*^[59] and Cheng *et al.*^[27] In these two studies, the fluorine ion was incorporated into the apatite structure throughout a complicated wet process^[59] and an alkoxide-based sol-gel technique,^[27] respectively. In the latter,^[27] the fluorine ion content of FHA coatings with 33.3, 66.6, and 100 pct theoretical degree of fluoridation was measured in the outer surface layer and the bulk of the coating by XPS and pF-meter analysis techniques, respectively. None of the calculated fluorine content matched the theoretical degree of fluoridation, but the results of XPS analysis were close to the theoretical degree of fluoridation. However, the use of the XPS technique to analyze F^{-1} ion content in the apatite structure is not a good choice, since it is well known that the XPS technique could only determine the chemical composition of the surface layer in depths less than 10 nm,^[61] not the chemical composition of the bulk material. Therefore, the results of XPS study reported by Cheng *et al.*^[27] could not be reliable to determine the fluorine content of the bulk material.

Wang *et al.*^[28] reported a constant ratio of F/Ca equal to 0.125, corresponded to 62.5 pct of fluorination, for electrodeposited FHA coatings with a theoretical degree of fluoridation higher than 62.5 pct. They concluded that in the electrochemical deposition technique, there is a limit in the maximum amount of F^{-1}

ion that can be incorporated into the apatite lattice. Based on this report, the maximum amount of OH^{-1} ions that could be successfully replaced by F^{-1} ions *via* the electrochemical technique is 62.5 pct ($x = 1.25$), even if the designed amount of F^{-1} ions in the electrolyte could be suitable for a higher level of fluoridation.^[28] They also reported a linear relationship between the concentration of F^{-1} in the electrolyte and real fluorine content of the electrochemically deposited FHA when the designed degree of fluoridation was not higher than 62.5 pct.^[28] This is in good agreement with our results for method A and the mechanical alloying technique. It is plausible to claim that the performance of the modified sol-gel technique, method A, is better than the common wet methods and alkoxide-base sol-gel technique from the incorporation of fluorine ions into the apatite structure point of view, since all designed amounts of fluorine ions were incorporated into the apatite structure.

In order to evaluate the purity of the sol-gel derived FHA powders, trace elements in the nanopowders were measured *via* the ICP-OES chemical analysis technique and compared with ASTM 1185-88^[33] limits. In this standard, the concentration of Cd, As, Hg, and Pb should be limited to 5, 3, 5, and 30 ppm, respectively. Also, the total amount of heavy elements should be limited to 50 ppm. The amounts of trace elements (ppm) of sol-gel derived FHA powders were measured as follows: Ba0.013, Mg0.020, Pb0.017, Zn0.035, and other ions were not detected. The amount of Fe in the powders synthesized through method A was less than the detection limit, but in the powders produced *via* method B, it was 0.011 ppm. Fe could probably be an impurity in the nitric acid, which was added into the mixture to adjust the pH in method B. The sol-gel derived FHA powders could fulfill the requirements of ASTM 1185-88 standard to be used as a biomaterial in biomedical applications such as drug and nonviral gene delivery systems. Considering the trace element analysis of the mechanical alloying synthesized FHA powders, discussed in a previous report,^[29] in terms of powder purity, the sol-gel route compares favorably to the mechanical alloying method.

G. SEM Analysis

SEM photomicrographs of the FHA100 sample (method A) at two magnifications (4000 and 16,000 times) can be seen in Figures 9(a) and (b). Figure 9(a) shows that powders morphology consists of a distribution of fine agglomerates/particles, mainly with a size less than 100 nm, distributed on the surface of flakelike larger agglomerates. At 16,000 times magnification (Figure 9(b)), it is clear that accumulated fine particles and laminates with a polygonal shape were interconnected into the surface of flakelike larger agglomerates. The sol-gel derived nanopowders have a strong tendency to be agglomerated and form large agglomerates because of the various processes occurring during aging and drying of the gel and the nature of the sol-gel process as a down-top approach in the synthesis of nanomaterials.

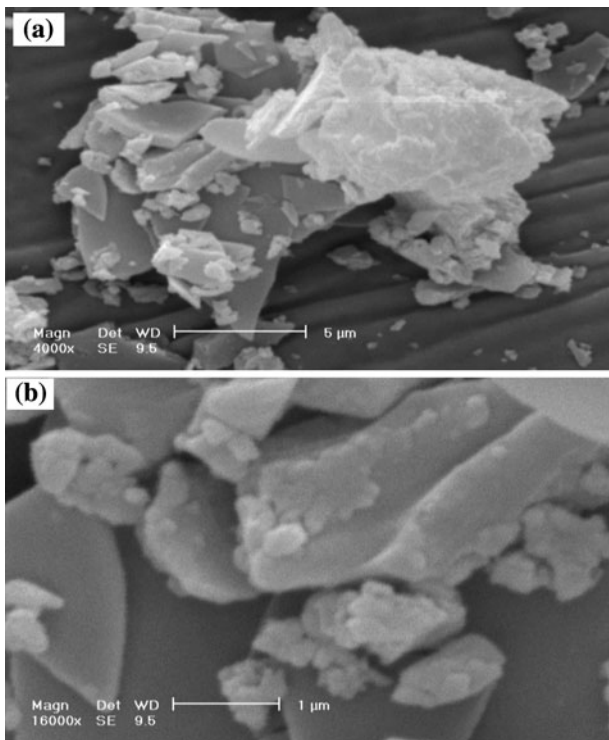


Fig. 9—SEM photomicrographs of the sol-gel derived FHA100 nanopowder, calcined at 873 K (600 °C) after 24 h of aging, which show the morphology of the nanopowder at different magnifications (method A).

H. TEM Analysis

TEM was used to examine and estimate the synthesized FHA100 powder particle sizes. Figures 10(a) and (b) present TEM photomicrographs for FHA100 synthesized nanopowders, after optimum aging time (24 hours) and calcination at 873 K (600 °C), and particle size distribution and morphology of the particles are clearly visible in these images, indicating the nanocrystalline nature of the powders. Nanoparticles obtained in method B are more agglomerated than the products of method A. In Figure 10(b), one of the agglomerates with 110-nm size, which consists of sub-structure of nanoparticles of about 47 nm in size, is shown at a higher magnification. Particle size distributions of the nanopowders, synthesized by methods A and B, were in the range of 20 to 30 nm and 40 to 70 nm, respectively. Based on this, the products of method A are more comparable to the size of the biological apatite.^[2]

The mean value of the calculated particle size, based on the TEM images, for FHA100 (product of method A) was in a good agreement with the value obtained from Scherer's formula (25.34 ± 2 nm); this match is evidence that no lattice strain was induced in the nanopowders during the synthesis process. The mean particle size value obtained from Scherer's formula for the FHA100 sample (33.12 ± 1.5 nm), synthesized by method B, did not match the mean value of particle size calculated based on TEM images (Figure 10(b)). When the Williamson–Hall formula^[62] was employed to

estimate the crystallite size of the FHA100 powder produced by method B, the crystallite size was about 56.7 nm, which was close to the mean value of the particle size estimated based on TEM images for the FHA100 sample (method B). Calculated lattice strain for this sample, using the Williamson–Hall formula, was equal to 0.1 pct.

The selected area electron diffraction (SAED) patterns (Figures 10(c) and (d)) show spotted sharp and continuous rings typically exhibited by polycrystalline grains. These reflections (spots) originated from individual particles. All of the reflections could be indexed according to the FA structure. The reflections of the experimental pattern are connected to rings at the positions where the calculated powder diffraction pattern shows the highest intensity: (210), (211), and (213). Those positions were marked on the experimental diffraction pattern in Figure 10(d). The reflections are broadened and diffuse, due to the small particle size.

I. FHA Coating Preparation

Figure 11 shows XRD patterns of sol-gel derived FHA coatings with different degrees of fluoridation after 24 hours of aging and calcination at 873 K (600 °C) for 1 hour. In all patterns, the characteristic peaks of well-crystallized apatite could be identified and there was no trace of β -TCP, TTCP, or CaF_2 . In terms of relative intensity and position of the peaks, there was a good match between the characteristic apatite peaks in FHA0 and FHA100 XRD patterns with the standard JCDP card of HA (JCDP 09-0432)^[47] and FA (JCDP 15-0876),^[42] respectively. Also, some sets of reflections shifted toward the right-hand side and (211) and (112) peaks merged with the increasing fluoridation level, which is in good agreement with the results presented in Figure 4. Moreover, the peak intensity appeared to increase with the increasing amount of fluorine ion incorporation into the apatite structure, but the difference was not considerable. Another observation was the broadening of the peaks in the XRD patterns. Calculated crystallite sizes of the FHA coatings, using Eq. [1], are presented in Table III and compared with the crystallite size of the sol-gel derived FHA nanopowders, discussed in Section D (Figure 4). For each FHA compound, there is a difference between the crystallite size of the coating and powders considering the fact that the calcination time and temperature were similar. In this experiment, the tendency of FHA ceramic for grain growth during the calcination step was high for FHA coatings compared to the FHA nanopowders. An upward trend in crystallite size, when there is an increase in the level of fluoridation, can be seen in both nanocrystalline coatings and powders.

The surface morphology of FHA100 coating after calcination at 873 K (600 °C), without aging, can be seen in Figures 12(a) through (c). Figures 13(a) through (f) show the surface morphology of FHA0, FHA25, FHA50, FHA75, and FHA100 after 24 hours of aging and calcination at 873 K (600 °C) for 1 hour. Coating without aging had a nonuniform surface morphology (Figure 12), and on the surface of FA coating without

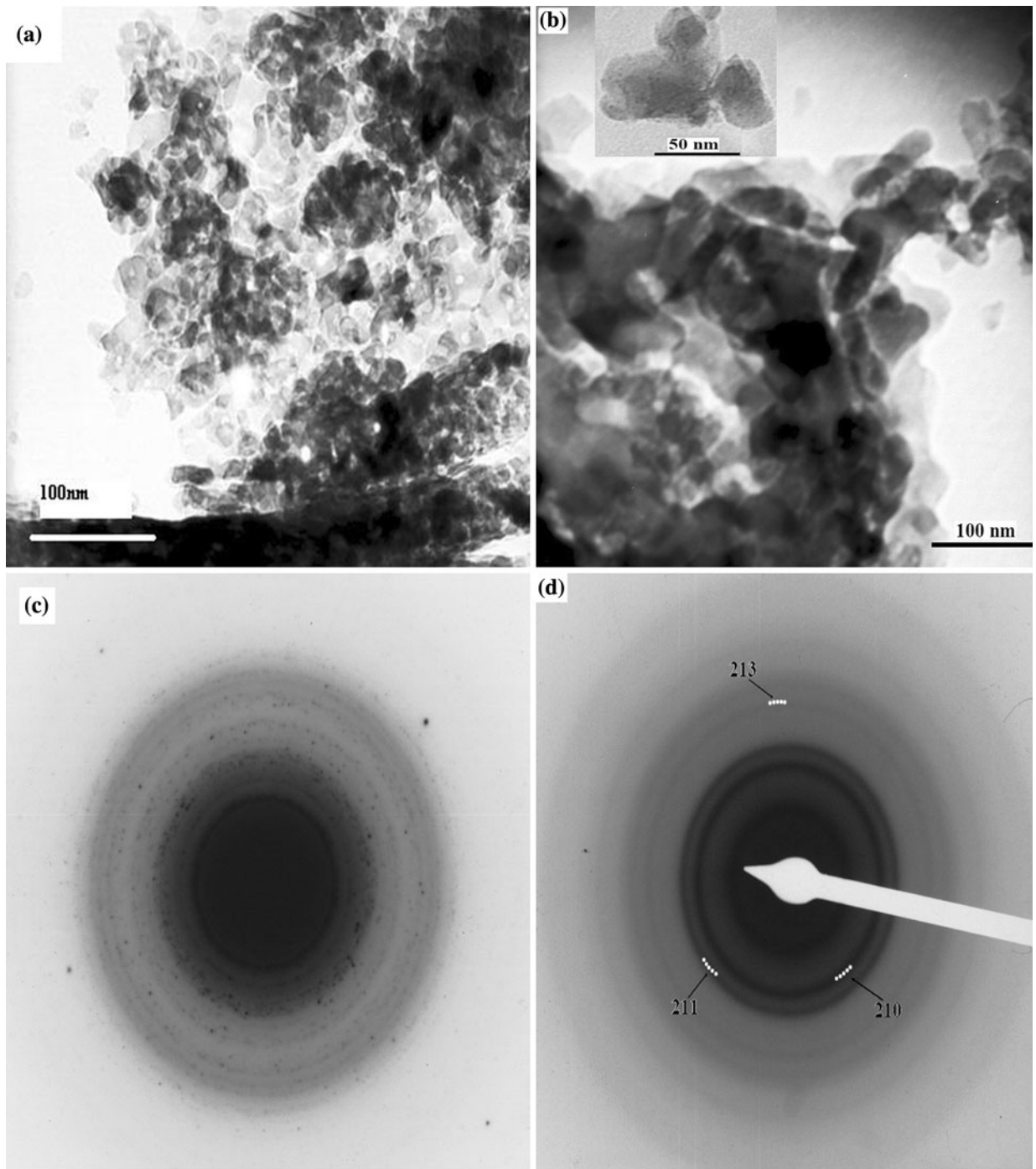


Fig. 10—TEM photomicrographs of FHA100 samples synthesized by (a) method A and (b) method B, and SAED patterns of FHA100 samples synthesized through (c) method B and (d) method A, after optimum aging time (24 h) and calcination at 873 K (600 °C).

aging, microcracks and delamination of the coating (Figures 12(a) and (b)) as well as a continuous network of voids and pits with a diameter less than 400 nm (Figure 12(c)) can be observed, scattered throughout the structure. After 24 hours of aging (Figure 13), the surface became dense, uniform, and homogenous with the absence of cracks, delamination, and voids and the particles of the coatings were densely compacted (Figures 13(e) and (f)). The surface morphology of the

FHA0 coating is different from the other samples. The FHA25 coating had the smoothest surface and became rougher with an increase in the level of fluoridation. On the surface of the FHA100 coating at 8000 times magnification (Figure 13(f)), nanopores can be observed.

The presence of porosity with a diameter less than 10 μm promotes body fluid circulation and cell migration to the core of the implant, and it could

provide a scaffold for bone-cell colonization around the implant.^[63] Hwang *et al.*^[64] suggested that the surface morphology and crystallization of the coating produced

through the sol-gel technique could be affected by the presence of residual organic compounds such as carbon. Carbon is the main element in the chemical composition of absolute ethanol as the solvent, and other impurity phases remained in the final gel as a result of incomplete reaction between the precursors during the mixing step (Figure 3(a)). Vaporization and phase change of these organic residues during calcination of FA coating without aging could cause the formation of delamination, cracks, and voids in the coating. Therefore, proper aging of the sol (24 hours) before dip coating is critically

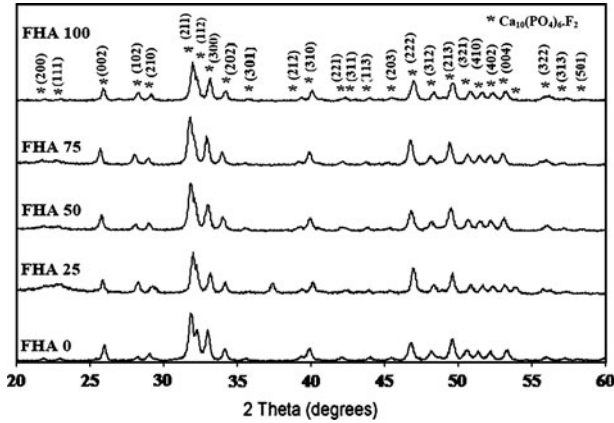


Fig. 11—XRD patterns of sol-gel derived FHA0, FHA25, FHA50, FHA75, and FHA100 nanostructured coatings, after 24 h of aging and calcination at 873 K (600 °C) for 1 h.

Table III. Calculated Crystallite Size of FHA0, FHA25, FHA50, FHA75, and FHA100 Nanopowders (Method A) and Nanostructured Coatings (24 h of Aging and Calcination at 873 K (600 °C) for 1 h)

Sample Condition	FHA0	FHA25	FHA50	FHA75	FHA100
Coating	33 (1)	36 (0.3)	39 (1)	41.6 (1.5)	44 (1)
Powder	19 (0.5)	20.6 (1)	22 (0.8)	24 (1)	25.3 (2)

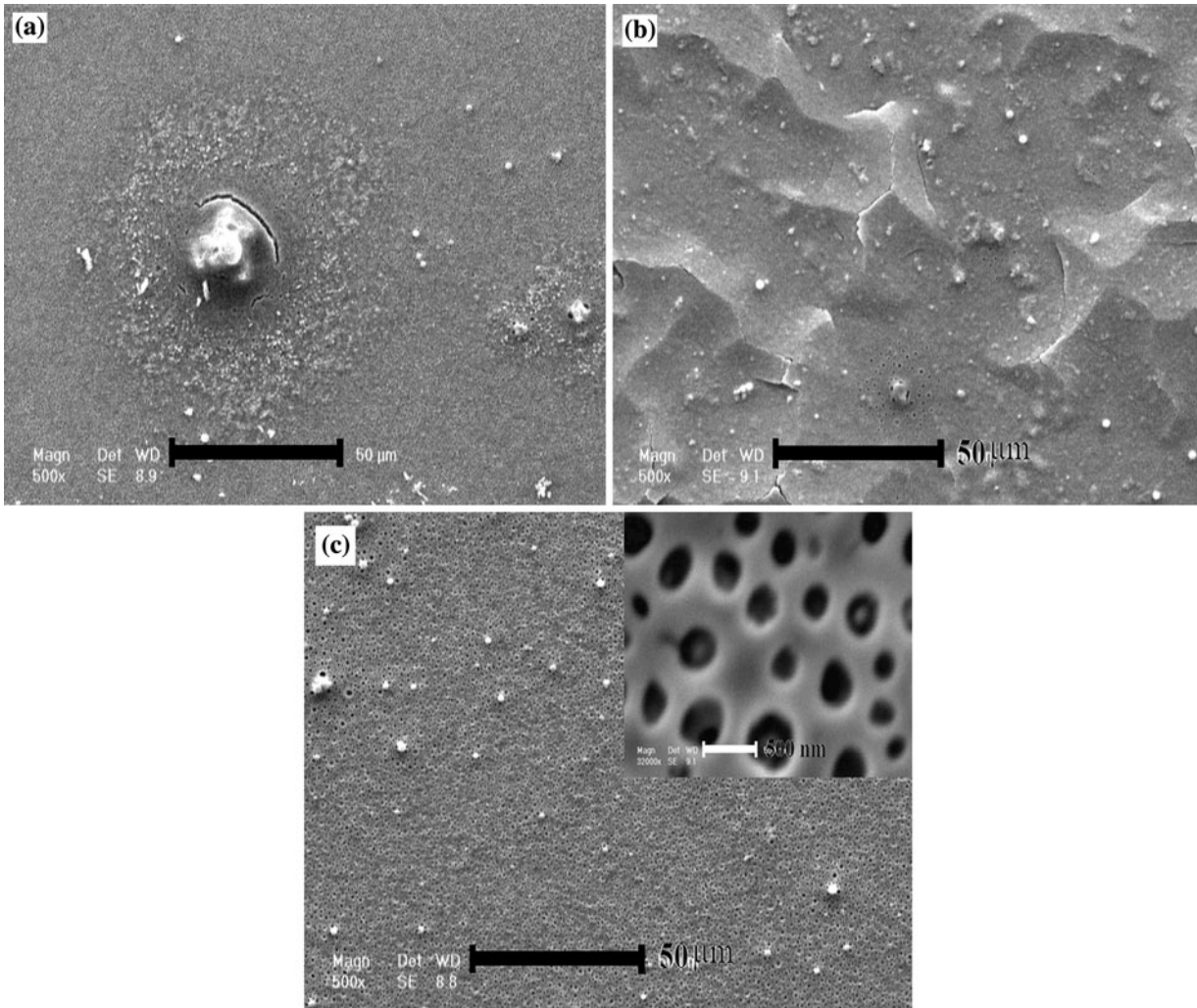


Fig. 12—SEM photomicrographs of the FHA100 surface coating morphology without aging, after calcination at 873 K (600 °C) for 1 h, at different magnifications.

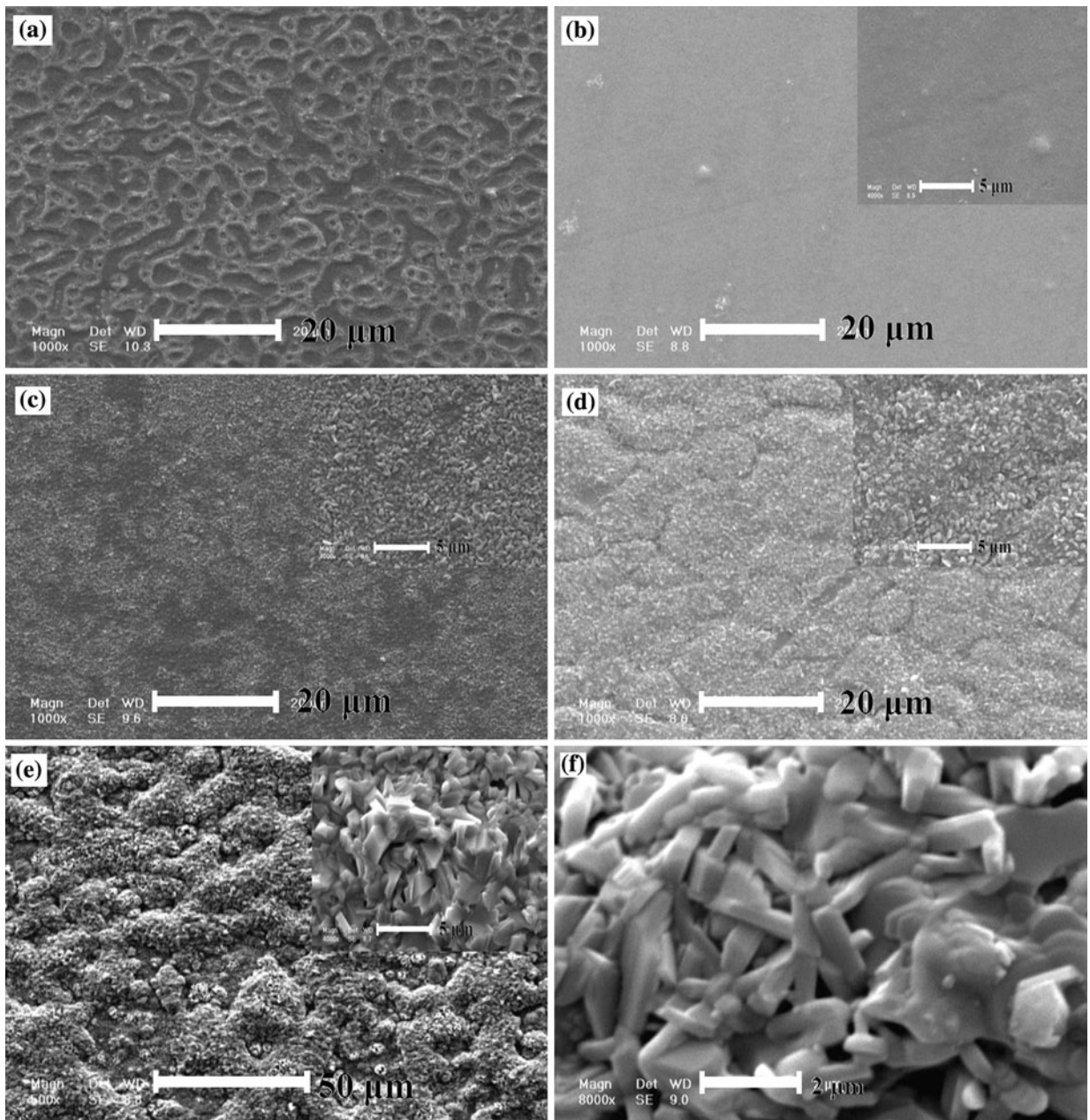


Fig. 13—SEM photomicrographs of (a) FHA0, (b) FHA25, (c) FHA50, (d) FHA75, and (e) and (f) FHA100 surface coating at different magnifications, which shows the morphology of the coatings obtained after 24 h of aging and calcination at 873 K (600 °C) for 1 h.

important to allow chemical reactions to reach completion at ambient temperature in order to avoid delamination and cracking of the coating and to achieve a coating with satisfactory morphology and adherence.

Cross-sectional morphology of FHA100 coating after 24 hours of aging and calcination at 873 K (600 °C) for 1 hour is shown in Figures 14(a) through (c). SEM analysis confirmed that a smooth, fully dense, well-compacted, crack-free, and uniform FA layer with a mean thickness of $40 \pm 5 \mu\text{m}$ was formed on 316L stainless steel substrate. FA coating adhered well on the surface of the substrate, and no gap in the interface or delamination could be detected. This implies that the bonding between the coating and substrate is strong

enough to have good performance during implantation. Cheng *et al.* prepared an FHA coating with a thickness of $1.5 \mu\text{m}$ on metallic substrate after 5 times repeat of the deposition process using the alkoxide-based sol-gel technique (similar to method B of this study)^[27] and organic precursors. Kim *et al.* successfully deposited an FHA coating with a thickness of $1 \mu\text{m}$ on zirconia substrate^[14] and a thickness of $5 \mu\text{m}$ on cp-Ti *via* inorganic precursors.^[15] In comparison with the work of these researchers, in the current study, nanostructured, crack-free, uniform, and dense FHA coatings, $45 \mu\text{m}$ in thickness, with good adherence on the substrate, were deposited on 316L stainless steel through a simpler sol-gel technique.

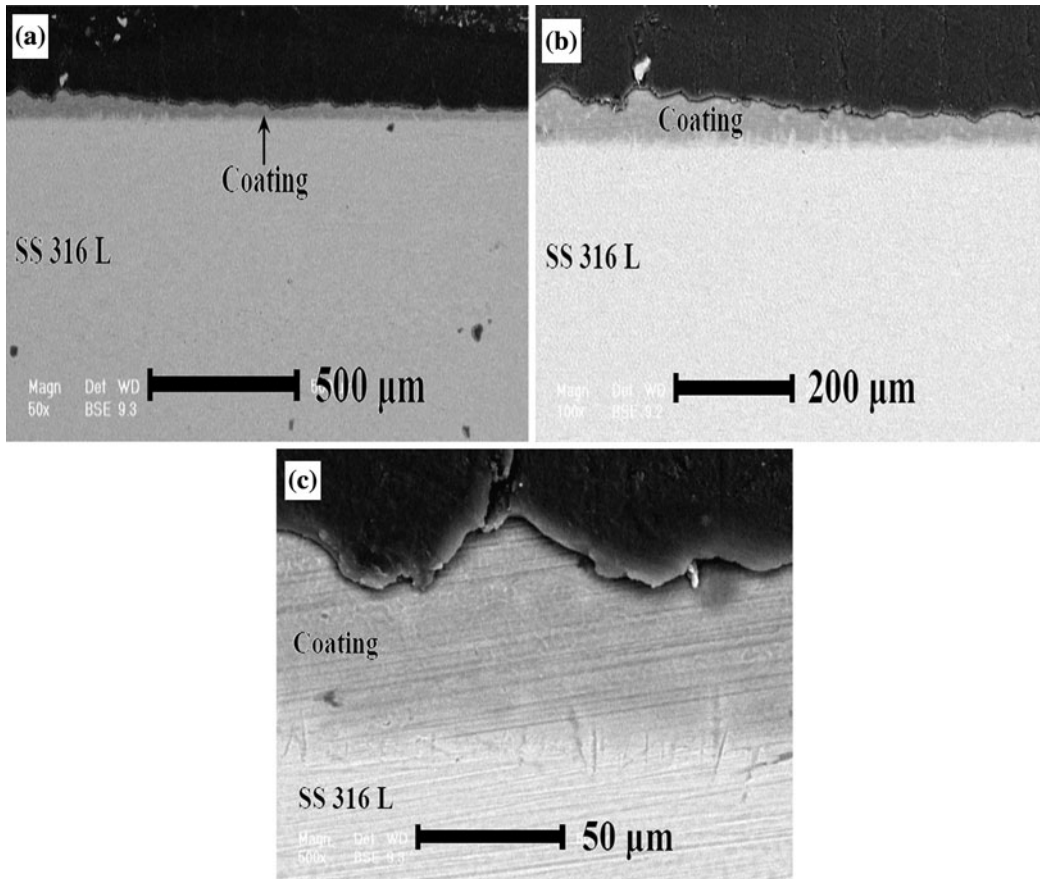


Fig. 14—SEM photomicrographs of the FHA100 surface coating cross section prepared after 24 h of aging and calcination at 873 K (600 °C) for 1 h at different magnifications.

IV. CONCLUSIONS

Single-phase pure nanocrystalline FHA powders with 0, 25, 50, 75, and 100 pct replacement of hydroxyl groups by fluorine ions and 20 to 25 nm in size, which were able to fulfill the requirements of ASTM F1185-88 standard specification to be used in biomedical application, were synthesized through a modified simple sol-gel technique. Calcination for 1 hour at 873 K (600 °C) in stagnant air, after 24 hours of aging, was necessary to generate pure nano-FHA. Moreover, nanostructured, crack-free, uniform, and dense FHA coatings with good adherence on the substrate and almost 45 μm in thicknesses were deposited on 316L stainless steel through the modified sol-gel method. A maturing period (24 hours) was necessary to avoid delamination of the coating and to prevent the formation of cracks and voids on the surface coating structure.

In comparison with the alkoxide-based sol-gel technique, the particle size of the FHA powders decreased and crystallinity rose in the modified sol-gel technique since a lower molecules cross-linking network formed during the gelation step. In the modified sol-gel technique, reactions during the mixing step were significantly improved by elimination of the precursor hydrolysis step, and optimum aging time decreased. Aging time was effective in the phase composition, crystallinity, and particle size of the product. Gelation

kinetic of the FHA sols prepared through this simple technique was faster than the alkoxide-based sol-gel route because of a faster polymerization without a catalyst. FTIR analysis, lattice parameters calculation, and quantitative fluorine content measurements showed that the complete fluoridation of apatite occurs in the modified sol-gel route. TEM results confirmed that agglomeration of nanoparticles in the modified sol-gel technique was significantly less than the alkoxide-based sol-gel route. Better reproducibility, high yield, simplicity of process, and absence of catalyst to facilitate the gelation process make this modified technique very competitive with the other developed sol-gel processes and suitable for scaling up to industrial size.

The results of this study confirmed that the FHA formation mechanism in the alkoxide-based technique, based on the formation of nano-CaF₂ at the beginning of the mixing step, could not explain the formation of FHA in the newly developed modified sol-gel technique. The focus of future work will be to understand the mechanism of FHA formation through this new technique.

ACKNOWLEDGMENTS

One of the authors (EMZ) expresses his gratitude toward the Natural Science and Engineering Research

Council of Canada (NSERC) for providing a Vanier Canada Graduate Scholarship for him to pursue his Ph.D. in materials engineering at the University of British Columbia.

REFERENCES

- C. Drouet, F. Bosc, M. Banu, C. Largeot, C. Combes, G. Dechambre, C. Estournès, G. Raimbeaux, and C. Rey: *Powder Technol.*, 2009, vol. 190, pp. 118–22.
- L.L. Hench and J. Wilson: *Introduction to Bioceramics*, World Scientific, Singapore, 1993.
- S. Cazolabou, C. Combes, D. Eichert, and C. Rey: *J. Mater. Chem.*, 2004, vol. 14, pp. 2148–53.
- S. Kannan, J.H.G. Rocha, and J.M.F. Ferreira: *J. Mater. Chem.*, 2006, vol. 16, pp. 286–91.
- R. Murugan, T.S. Sampath, and K. Panduranga: *Mater. Lett.*, 2002, vol. 57, pp. 429–33.
- H.B. Pan and B.W. Darvell: *Arch. Oral Biol.*, 2007, vol. 52, pp. 861–68.
- P. Leamy, P.W. Brown, K. Tenhuisen, and C. Randall: *J. Biomed. Mater. Res.*, 1998, vol. 42, pp. 458–64.
- Y. Chen and X. Miao: *Biomaterials*, 2005, vol. 26, pp. 1205–10.
- A. Bianco, I. Cacciotti, M. Lombardi, L. Montanaro, E. Bemporad, and M. Sebastiani: *Ceram. Int.*, 2010, vol. 36, pp. 313–22.
- Q. Xiang, Yong Liu, X. Sheng, and X. Dan: *Dent. Mater.*, 2007, vol. 23, pp. 251–58.
- S. Kannan, J.H.G. Rocha, S. Agathopoulos, and J.M.F. Ferreira: *Acta Biomater.*, 2007, vol. 3, pp. 243–49.
- H.U. Lee, Y.S. Jeong, S.Y. Park, S.Y. Jeong, H.G. Kim, and C.R. Cho: *Curr. Appl. Phys.*, 2009, vol. 9, pp. 528–33.
- H. Kim, E. Lee, H.E. Kim, V. Salih, and J.C. Knowles: *Biomaterials*, 2005, vol. 26, pp. 4395–404.
- H.W. Kim and Y.M. Kong: *Biomaterials*, 2004, vol. 25, pp. 2919–26.
- H.W. Kim and Y.M. Kong: *Biomaterials*, 2004, vol. 25, pp. 3351–58.
- J.R. Farley, J.E. Wergedal, and D.J. Barlink: *Science*, 1983, vol. 222, pp. 330–32.
- B.Y. Reed, J.E. Zerwekh, and P.P. Antich: *J. Bone Miner. Res.*, 1993, vol. 8, pp. 19–25.
- D. Yan, A. Gurumurthy, M. Wright, T. Wayne, E.G. Lobo, and E.T. Everett: *Bone*, 2007, vol. 41, pp. 1036–44.
- E. Bertoni, A. Bigi, G. Cojazzi, M. Gandolfi, S. Panzavolta, and N. Roveri: *J. Inorg. Biochem.*, 1998, vol. 72, pp. 29–35.
- E.Z. Kurmaev, S. Matsuya, S. Shin, M. Watanabe, R. Eguchi, Y. Ishiwata, T. Takeuchi, and M.J. Iwami: *J. Mater. Sci.: Mater. Med.*, 2002, vol. 13, pp. 33–37.
- L.M. Rodriguez-Lorenzo, J.N. Hart, and K.A. Gross: *Biomaterials*, 2003, vol. 24, pp. 3777–85.
- Z. Lu, H. Wang, J. Zeng, and J. Liu: *J. Cryst. Growth*, 2009, vol. 311, pp. 4791–98.
- H. Qu and M. Wei: *J. Mater. Sci.: Mater. Med.*, 2005, vol. 16, pp. 129–33.
- K. Cheng, S. Zhang, and W. Weng: *J. Sol-Gel Sci. Technol.*, 2006, vol. 38, pp. 13–37.
- K. Cheng, G. Han, W. Weng, H. Qu, P. Du, J. Yang, and J.M.F. Ferreira: *Mater. Res. Bull.*, 2003, vol. 38, pp. 89–97.
- K. Cheng, G. Shen, W. Weng, G. Han, J.M.F. Ferreira, and J. Yang: *Mater. Lett.*, 2001, vol. 51, pp. 37–41.
- K. Cheng, S. Zhang, and W. Weng: *Surf. Coat. Technol.*, 2005, vol. 198, pp. 237–41.
- J. Wang, Y. Chao, Q. Wanb, Z. Zhu, and H. Yu: *Acta Biomater.*, 2009, vol. 5, pp. 1798–1807.
- M.H. Fathi and E. Mohammadi Zahrani: *J. Cryst. Growth*, 2009, vol. 311, pp. 1392–403.
- G. Bezzi, G. Celotti, E. Landi, T.M.G. La Torretta, I. Sopyan, and A. Tampieri: *Mater. Chem. Phys.*, 2003, vol. 78, pp. 816–24.
- B.D. Cullity: *Elements of X-Ray Diffraction*, 2nd ed., Addison-Wesley Publishing, Reading, MA, 1977.
- E. Landi, A. Tampieri, G. Celotti, and S. Sprio: *J. Eur. Ceram. Soc.*, 2000, vol. 20, pp. 2377–87.
- ASTM Standard Specification for Composition of Ceramic Hydroxyapatite for Surgical Implants*, F1185–88, ASTM, Philadelphia, PA, 1988, p. 415.
- C.J. Brinker and G.W. Scherer: *Sol-Gel Science*, Academic Press, Boston, MA, 1990.
- D.M. Liu, T. Troczynski, and W.J. Tseng: *Biomaterials*, 2001, vol. 22, pp. 1721–30.
- A. Bigi, E. Boanini, and K. Rubini: *J. Solid State Chem.*, 2004, vol. 177, pp. 3092–98.
- S. Kim and P.N. Kumta: *Mater. Sci. Eng. B*, 2004, vol. 111, pp. 232–36.
- D.M. Liu, T. Troczynski, and W.J. Tseng: *Biomaterials*, 2002, vol. 23, pp. 1227–36.
- M.H. Fathi and A. Hanifi: *Adv. Appl. Ceram.*, 2009, vol. 108, pp. 363–68.
- L. Calderin and M.J. Stott: *Phys. Rev.*, 2003, vol. 67, pp. 134106–10.
- S. Cazolabou, C. Combes, D. Eichert, and C. Rey: *J. Mater. Chem.*, 2004, vol. 14, pp. 2148–53.
- JCPDS File No. 15-0876 (Fluorapatite), Joint Committee on Powder Diffraction Standards, Swathmore, PA, 1988.
- A.J. Ruys, K.A. Zeigler, O.C. Standard, A. Brandwood, B.K. Milthorpe, and C.C. Sorrell: in *Proceedings for the International Ceramic Conference. AUSTCERAM-92*, M.J. Bannister, ed., CSIRO, Melbourne, 1992, vol. 2, pp. 605–10.
- C.M. Lopatin, V. Pizziconi, T.L. Alford, and T. Laursen: *Thin Solid Films*, 1998, vol. 326, pp. 227–32.
- M. Kay, R.A. Young, and A.S. Posner: *Nature*, 1964, vol. 204, pp. 3056–65.
- M. Wei, J.H. Evans, T. Bostrom, and L. Grndahl: *J. Mater. Sci.: Mater. Med.*, 2003, vol. 14, pp. 311–20.
- JCPDS File No. 09-0432 (Hydroxyapatite), Joint Committee on Powder Diffraction Standards, Swathmore, PA, 1988.
- M.H. Fathi and E. Mohammadi Zahrani: *J. Alloys Compd.*, 2009, vol. 475, pp. 408–14.
- J.P. Lafon, E. Champion, and D. Bernache: *J. Eur. Ceram. Soc.*, 2008, vol. 28, pp. 139–47.
- R. Murugan and S. Ramakrishna: *J. Cryst. Growth*, 2005, vol. 274, pp. 209–13.
- H. Zhang, Q. Zhu, and Z. Xie: *Mater. Res. Bull.*, 2005, vol. 40, pp. 1326–34.
- F. Freund and R.M. Knobel: *Dalton Trans., J. Chem. Soc.*, 1977, vol. 6, pp. 1136–40.
- C. Rey, J.L. Miquel, L. Facchini, A.P. Legrand, and M.J. Glimcher: *Bone*, 1995, vol. 16, pp. 583–86.
- M.G. Taylor, S.F. Parker, K. Simkiss, and C.H. Mitchell: *Phys. Chem. Chem. Phys.*, 2001, vol. 3, pp. 1514–17.
- M. Okazaki, H. Tohda, T. Yanagisawa, M. Taira, and J. Takahashi: *Biomaterials*, 1998, vol. 19, pp. 611–16.
- J. Kazimiroff, S.R. Frankel, and R.Z. LeGeros: *Bioceramics*, 1996, vol. 9, pp. 169–72.
- T. Sakae, A. Ookubo, and R.Z. LeGeros: *Key Eng. Mater.*, 2003, vol. 240, pp. 395–98.
- F. Yao, J.P. LeGeros, and R.Z. LeGeros: *Acta Biomater.*, 2009, vol. 5, pp. 2169–77.
- K.A. Gross and L.M. Rodriguez-Lorenzo: *Biomaterials*, 2004, vol. 25, pp. 1375–84.
- E. Mohammadi Zahrani and M.H. Fathi: *Ceram. Int.*, 2009, vol. 35, pp. 2311–23.
- F.M. Amanullah, K.J. Pratap, V. Hari Babu, and V. Hari Babu: *Mater. Sci. Eng. B*, 1998, vol. 52, pp. 93–98.
- K. Williamson and W.H. Hall: *Acta Metall.*, 1953, vol. 1, pp. 22–31.
- A. Ravaglioli and A. Krajewski: *Bioceramics: Materials, Properties, Applications*, Chapman and Hall, London, 1992.
- K. Hwang and Y. Lim: *Chemical: Surf. Coat. Technol.*, 1999, vol. 115, pp. 172–75.